Article

Current Biology

A mismatch in the expression of cell surface molecules induces tissue-intrinsic defense against aberrant cells

Highlights

- Robos, Teneurins, and LRR proteins confer detection of abnormal neighboring cells
- An expression level mismatch between adjacent cells triggers "interface surveillance"
- Robo2 and Robo3 activate interface surveillance independent of the ligand Slit
- Fate-patterning pathways establish a cell surface profile unique to each cell fate

Authors

Friedericke Fischer, Laurin Ernst, Anna Frey, ..., Vanessa Weichselberger, Ramya Balaji, Anne-Kathrin Classen

Correspondence

anne.classen@biologie.uni-freiburg.de

In brief

Fischer et al. find that *Drosophila* tissues rely on a cell surface code of Robo receptors, Teneurins, and other LRR proteins to identify abnormal neighboring cells with deregulated developmental fate, including activation of oncogenic Ras. Cell identification depends on expression differences, leading to cell elimination by "interface surveillance."

Fischer et al., 2024, Current Biology *34*, 980–996
March 11, 2024
https://doi.org/10.1016/j.cub.2024.01.053

CellPress

CellPress
OPEN ACCESS

Current Biology

Article

A mismatch in the expression of cell surface molecules induces tissue-intrinsic defense against aberrant cells

Friedericke Fischer,[1,2,3] Laurin Ernst,[1,2,3] Anna Frey,[1,2,4] Katrin Holstein,[5] Deepti Prasad,[1,2,4] Vanessa Weichselberger,[4,6] Ramya Balaji,[1,2] and Anne-Kathrin Classen[1,2,7,8,9,10,*]

[1]Hilde-Mangold-Haus, University of Freiburg, 79104 Freiburg, Germany
[2]Faculty of Biology, University of Freiburg, 79104 Freiburg, Germany
[3]International Max Planck Research School for Immunobiology, Epigenetics, and Metabolism, 79108 Freiburg, Germany
[4]Spemann Graduate School of Biology and Medicine (SGBM), University of Freiburg, 79104 Freiburg, Germany
[5]Department of Vascular Cell Biology, Max Planck Institute for Molecular Biomedicine, 48149 Münster, Germany
[6]Aix Marseille University, CNRS, UMR 7288, IBDM, 13288 Marseille, France
[7]CIBSS Centre for Integrative Biological Signalling Studies, University of Freiburg, 79104 Freiburg, Germany
[8]BIOSS Centre for Biological Signalling Studies, University of Freiburg, 79104 Freiburg, Germany
[9]X (formerly Twitter): @classenlab
[10]Lead contact
*Correspondence: anne.classen@biologie.uni-freiburg.de
https://doi.org/10.1016/j.cub.2024.01.053

SUMMARY

Tissue-intrinsic error correction enables epithelial cells to detect abnormal neighboring cells and facilitate their removal from the tissue. One of these pathways, "interface surveillance," is triggered by cells with aberrant developmental and cell-fate-patterning pathways. It remains unknown which molecular mechanisms provide cells with the ability to compare fate between neighboring cells. We demonstrate that *Drosophila* imaginal discs express an array of cell surface molecules previously implicated in neuronal axon guidance processes. They include members of the Robo, Teneurin, Ephrin, Toll-like, or atypical cadherin families. Importantly, a mismatch in expression levels of these cell surface molecules between adjacent cells is sufficient to induce interface surveillance, indicating that differences in expression levels between neighboring cells, rather than their absolute expression levels, are crucial. Specifically, a mismatch in Robo2 and Robo3, but not Robo1, induces enrichment of actin, myosin II, and Ena/Vasp, as well as activation of JNK and apoptosis at clonal interfaces. Moreover, Robo2 can induce interface surveillance independently of its cytosolic domain and without the need for the Robo-ligand Slit. The expression of Robo2 and other cell surface molecules, such as Teneurins or the Ephrin receptor is regulated by fate-patterning pathways intrinsic and extrinsic to the wing disc, as well as by expression of oncogenic Ras^{V12}. Combined, we demonstrate that neighboring cells respond to a mismatch in surface code patterns mediated by specific transmembrane proteins and reveal a novel function for these cell surface proteins in cell fate recognition and removal of aberrant cells during development and homeostasis of epithelial tissues.

INTRODUCTION

Genetically altered cells are constantly appearing in epithelial tissues, either because of developmental errors or mutagenesis.[1,2] Surveillance and removal of these cells is necessary to maintain tissue homeostasis and organismal health. "Interface surveillance"—a distinct branch of tissue-intrinsic error correction mechanisms, such as cell-cell competition—mediates the removal of aberrant cells from epithelial tissues.[3,4] Interface surveillance is specifically activated by aberrant cells that carry mutations in cellular signaling pathways or transcriptional networks, which control cell fate and differentiation programs. For example, mutations in patterning pathways (Decapentaplegic [Dpp]/TGF-β, Wingless [Wg]/WNT, Hedgehog (Hh)/Shh, JAK/STAT, and Notch) or in cell-fate-specifying transcription factors and transcriptional regulators (Arm, Iro-C, Omb, Yki, En/Inv, Ap, Ci, and Hox genes) induce phenotypes related to interface surveillance.[5–23] Mosaic clones that deregulate these pathways produce a pronounced difference in cell fate between "aberrant" and surrounding "normal" cells, and we have previously shown that such steep fate differences between neighboring cells cause enrichment of myosin II and filamentous actin at shared junctional and lateral interfaces in *Drosophila* imaginal epithelia. This drives cell segregation between the two cell populations via smoothening of the contractile interface, a characteristic feature of interface surveillance.[3] Importantly, this response is induced in a strictly position-dependent manner according to the cell fate of the surrounding cells. For example, Cubitus interruptus (Ci)-expressing clones have normal shapes in anterior wing compartments, where Ci-activation by Hh

CellPress
OPEN ACCESS

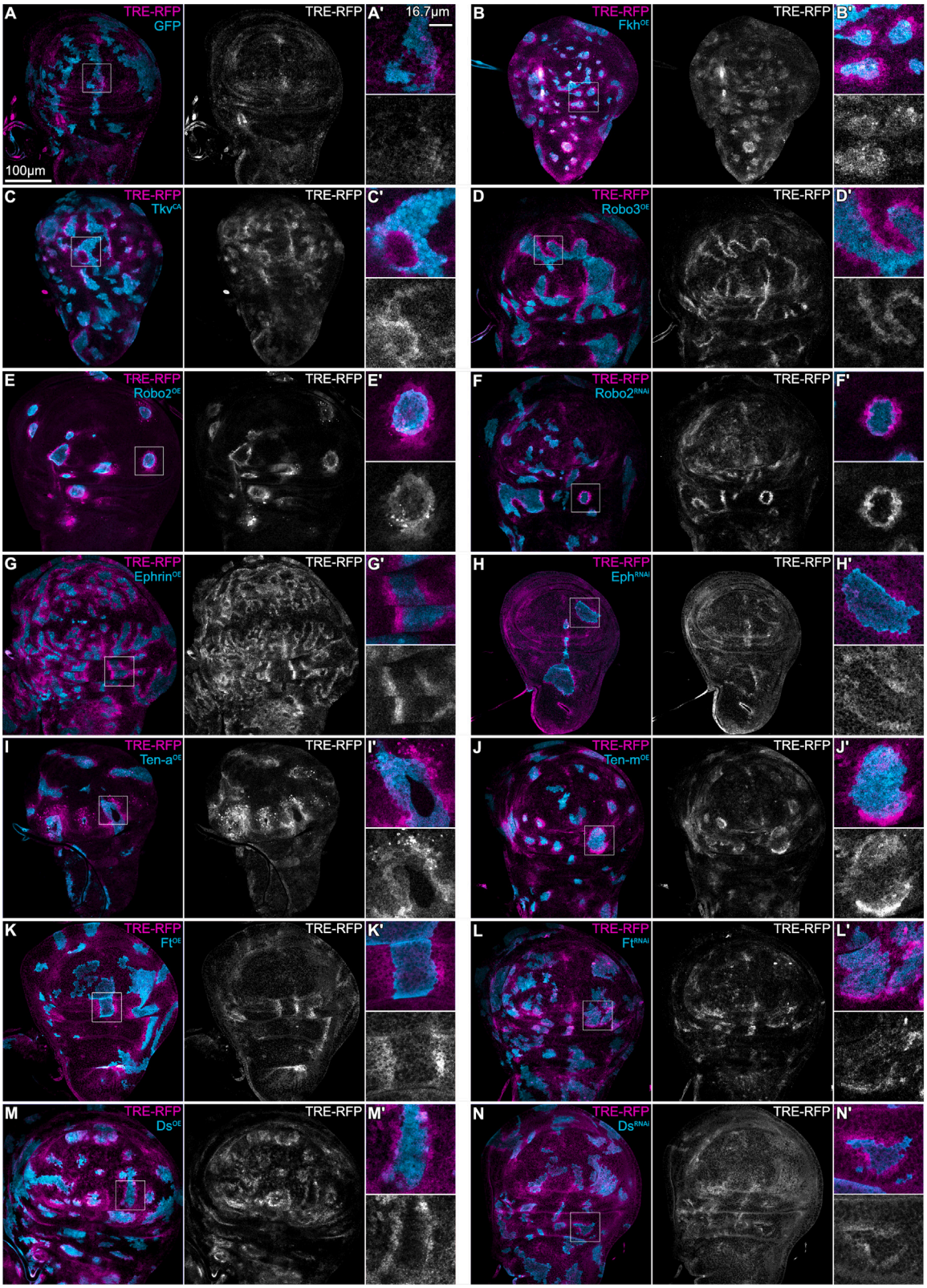

Figure 1. Cell surface molecules with described roles in axon guidance mediate cell-cell recognition in wing discs

TRE-RFP expression is reporting JNK pathway activity (gray or magenta in all panels).

(A) A mosaic wing disc with wild-type clones expressing *UAS-GFP* (GFP, cyan). Please note that JNK activity is physiologically elevated at the A/P compartment boundary in wing discs at this developmental stage. White frame marks region shown in (A′).

(legend continued on next page)

signaling is high. However, Ci-expressing clones undergo smoothening and die in posterior compartments, where Ci-signaling is normally low.[3] This emphasizes that it is the difference in fate at the clone interface, or in other words, the fate mismatch, rather than the fate per se, which is important for inducing interface surveillance. Curiously, actomyosin recruitment and interface smoothing bear a striking resemblance to the formation of compartment boundaries in developing tissues, where two cell populations of different fate are mechanically separated by the formation of a contractile actomyosin interface between them.[24–26] However, actomyosin enrichment in interface surveillance is also accompanied by activation of pro-apoptotic c-Jun N-terminal kinase (JNK) signaling in cells on either side of the clonal interface.[3,4] This drives apoptotic elimination of aberrant cells and is thus an essential hallmark of interface surveillance and its ability to maintain tissue health.

Despite this work, it is still unclear how cells recognize when a neighboring cell acquires a distinct and potentially aberrant fate. Recruitment of actomyosin to the interface and JNK activation in cells on both sides of the interface suggests that surveillance of neighbors is mediated by a cell-contact-dependent mechanism. The molecular machinery responsible for interface surveillance must therefore be composed of cell surface molecules, (1) which modulate actomyosin function and (2) which are competent to transduce contact-dependent signals into signaling pathways, such as JNK. Additionally, (3) expression of these molecules must be regulated by cell-fate-specifying transcription factors and pathways, thereby encoding cell identity. Classical cadherins are prime examples of transmembrane molecules that may fulfill these criteria.[27] Yet, the striking pattern-specific activation of interface surveillance, as for Ci-expressing clones, is observed for multiple fate-patterning pathways. This implies that more than one molecule is necessary to distinguish any two of many possible cell fates from each other.[3,4] Recently, novel and unexpected roles for members of the neuronal axon guidance and neuronal adhesion families emerged in physiology and pathology of epithelial tissues.[28,29] Axon guidance molecules typically mediate signaling through the interaction of a transmembrane receptor with a cognate ligand. Roundabout (Robo), Plexin, Frazzled (Fra), or Ephrin (Eph) receptor families interact with respective ligands of the Slit, Semaphorin (Sema), Netrin (Net), and Ephrin families.[30–33] Recent work suggests that Teneurins interact with leucine-rich repeat (LRR)-domain proteins on neighboring cell surfaces.[33,34] Extensive research on axon guidance effectors has revealed this general principle: when the ligand binds to the receptor, it elicits signals to recruit actomyosin modulators of the small GTPase family (Rho and Rac) and members of the Ena/Vasp, Abl, or Src pathways.[32] This leads to either formation or retraction of actin-based cellular protrusions, thereby driving attractive or repulsive behaviors during axon pathfinding and mediating appropriate spatial positioning of cells within neuronal systems. It is conceivable that expression of these molecules may also have a strong impact on actomyosin and adhesion dynamics in an epithelial tissue thereby regulating epithelial morphogenesis and homeostasis.[29,30,35] Indeed, Ephrin, Teneurins, and LRR-domain proteins including Toll-like receptors are strongly implicated in mechanical separation of cell populations at compartment boundaries via regulation of a contractile actomyosin interface in epithelial tissues of vertebrate and invertebrate species.[24–26,36,37]

The phenomenological similarities lead us to explore whether these molecules played a role in interface surveillance against aberrant cells. Importantly, the diverse fates created by developmental patterning in the imaginal disc made this tissue an ideal system to experimentally address the mechanisms of cell fate recognition. We find that neuronal cell surface molecules are widely expressed in epithelia, that misexpression of a single surface molecule is sufficient to induce all hallmarks of interface surveillance, and that these cell surface molecules are co-regulated by cell fate specification pathways.

RESULTS

Cell surface molecules with described roles in axon guidance mediate cell-cell recognition in wing discs

To understand whether epithelial tissues may use cell surface molecules to distinguish fates and detect aberrant cells, we first asked whether misexpression of proteins functioning in axon guidance, neuronal targeting, and cell adhesion is sufficient to induce interface surveillance hallmarks. Mosaic clones expressing aberrant fates generally induce actomyosin recruitment, apoptosis, and, importantly, bilateral JNK signaling at the interface between clonal and wild-type cells (Figures S1A–S1E).[4] We thus used bilateral activation of the JNK-activity reporter TRE-RFP as a readout for a targeted genetic screen.[38] Where possible, we analyzed overexpression, as well as RNAi-mediated downregulation of cell surface molecules using the mosaic GAL4/UAS flip-out system.[39] Strikingly, we found that deregulation of single members of 6 cell surface protein families was sufficient to induce TRE-RFP activation at clone boundaries in wing imaginal discs. Specifically, ectopic up- and downregulation of members of the Robo family (Robo 2 and 3), the Teneurin-family (Ten-a and Ten-m), atypical cadherins (Fat and Ds), the Eph/Ephrin-system, Netrins (Netrin-B), and the LRR proteins Toll-2, Toll-8, or Tartan was sufficient to induce bilateral JNK interface signaling (Figures 1 and S1F–S1J). Importantly, several protein

(B and C) Mosaic wing discs with clonal alterations in fate-specifying pathways by the ectopic expression of Fkh (Fkh^{OE}) and the expression of constitutively active Tkv (Tkv^{CA}) using the "GAL4/UAS flp-out" system. Please note the induction of bilateral JNK signaling at mosaic interfaces. White frame marks regions shown in (B′) and (C′).

(D–N) Mosaic wing discs with aberrant expression of cell surface molecules. Clones express GFP (cyan) and were exposed to either ectopic expression (^{OE}) of *UAS* constructs or downregulation of expression by *UAS-RNAi* (^{RNAi}) constructs for individual cell surface molecules, as indicated in each panel. White frame marks regions shown in (D′)–(R′).

Images in (A)–(N) are shown at the same scale. JNK responses in (A)–(C) have been observed in $n \geq 3$ experimental replicates for this study and previous studies.[4] JNK responses in (F), (H), and (J)–(L) have been observed in $n \geq 3$ experimental replicates for this study. JNK response in (G), (I), (M), and (N) has been observed in $n \geq 3$ wing discs in one experimental replicate, which corresponds to the initial candidate screen (see Figure S1F).

Related to Figure S1.

CellPress
OPEN ACCESS

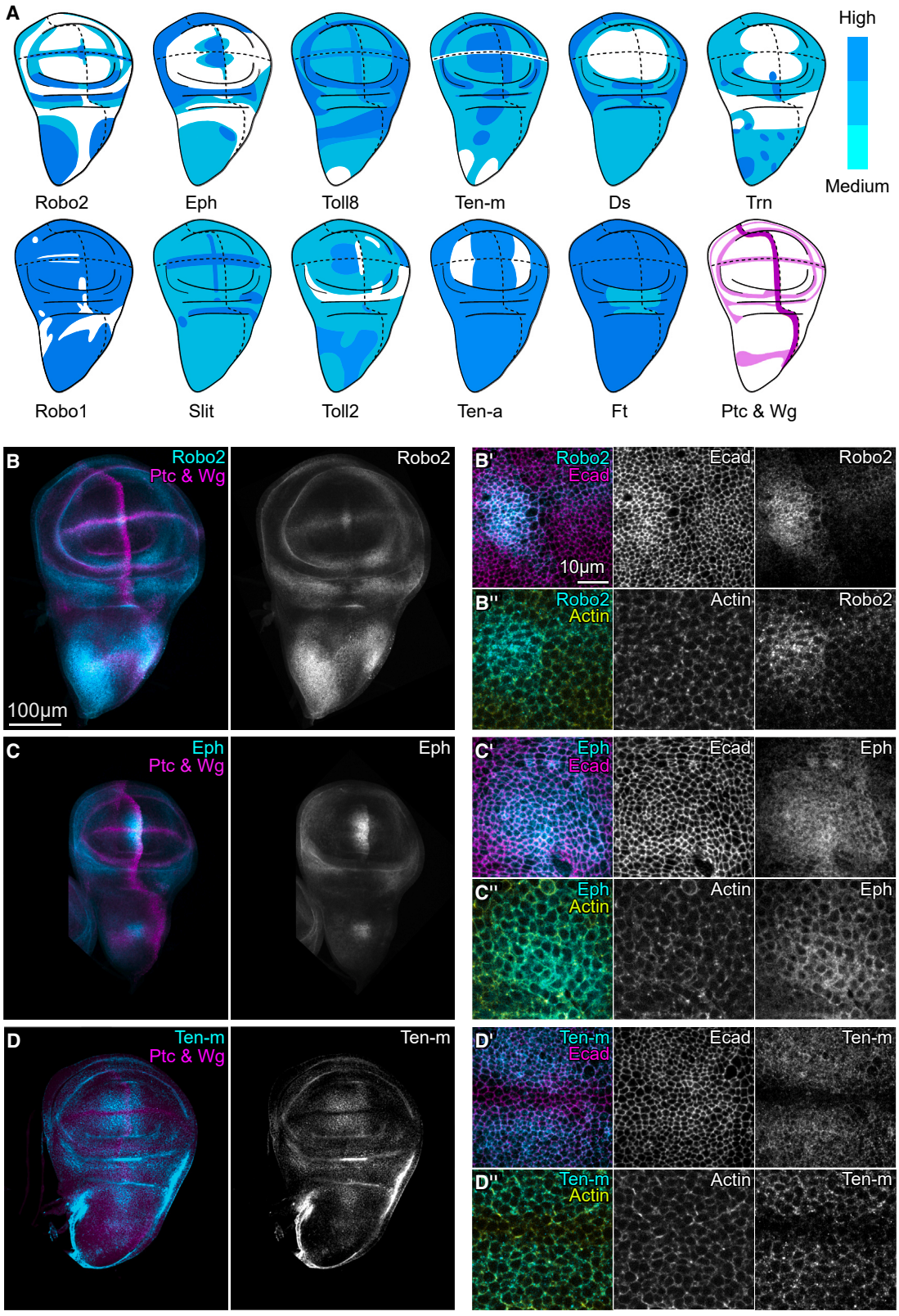

Figure 2. Cell surface molecules with described roles in axon guidance are expressed in wing disc epithelia

(A) Illustrations of expression patterns of cell surface molecules in third instar wing discs at 102 h after egg lay (AEL). Relative fluorescence intensity is depicted by color intensity from low (white), medium (cyan) to high (blue), see Figure S2 and experimental procedures. Expression domains of compartment boundary

(legend continued on next page)

families, such as members of the Plexin/Sema, Irre cell recognition module (IRM), and Dscam-families failed to score positively for JNK interface signaling in our screen, suggesting that not all cell surface molecules with roles in neuronal morphogenesis are involved in interface surveillance responses (Figure S1F). We conclude that a distinct set of cell surface molecules can mediate bilateral JNK signaling, otherwise a characteristic hallmark of interface surveillance toward cells with aberrant fate and specification programs. We thus wanted to examine whether these cell surface molecules may act as cell fate sensors required for the induction of interface surveillance.

Cell surface molecules with described roles in axon guidance are widely expressed in wing disc epithelia

To understand whether these cell surface molecules indeed play a role in aberrant cell recognition, we asked whether these proteins are physiologically expressed in wing discs. We analyzed their expression in early and late wing disc development using tools, such as antibodies, enhancer traps, or GFP-tagged proteins.[40,41] To provide a spatial reference, we included a staining for Patched (Ptc, anterior-posterior boundary) and Wg (dorsal-ventral boundary). We were surprised to find that most examined molecules were, indeed, expressed in wing discs, with increasingly complex expression patterns toward late 3rd instar stages (Figures 2A–2D and S2). Moreover, certain attributes of those patterns, such as an elevated expression in the pouch, hinge or notum suggest a possible regulation by well-described specification pathways in the wing disc (Figure S2B).[42] Consequently, each spatial position within the disc is endowed with a unique cell surface code, which, importantly, is composed of multiple different proteins (Figure 2A). The widespread expression of neuronal cell surface molecules suggests that these proteins may be linked to uncharacterized functions during development of imaginal discs.

To confirm that these proteins also locate to the cell surface in wing epithelia, we analyzed their subcellular distribution in more detail. Roundabout 2 (Robo2), Ephrin receptor (Eph), or Teneurin-m (Ten-m) localized to adherens junctions and lateral domains of wing disc cells (Figures 2B′–2D′′). Both adherens junctions and lateral surfaces establish contact between neighboring cells, and it is these surfaces that were previously shown to respond to the presence of aberrant cells by recruiting actomyosin.[3,4] Thus, Robo2, Eph, and Ten-m localize to cell surfaces that are implicated in activation of interface surveillance. Combined, these observations are consistent with a model where wing imaginal discs may utilize the combinatorial expression of cell surface molecules at adherens junctions and lateral surfaces to detect the fate and identity of neighboring cells.

A mismatch of Robo2 receptor expression levels between neighboring cells is detected by interface surveillance

Although atypical cadherins, Teneurins, Ephrin, and LRR proteins have emerging or even established roles in epithelial tissues, almost nothing is known about the epithelial function of Robo receptors.[36,37,43–45] We thus focused our further analysis on the three *Drosophila* Robo receptors Robo1, Robo2, and Robo3.

Because Robo2 is expressed throughout wing disc development (Figure 3G), we first analyzed the effects of mosaic manipulation of Robo2. We find that Robo2-expressing clones have smooth shapes, recruit actin to the interface and generally induce apoptosis (Figures 3A, 3B, 3D, and 3E). Moreover, the characteristic pattern of bilateral JNK signaling—where both wild-type cells and aberrant cells at the clonal interface activate JNK—can be detected around Robo2-expressing clones (Figures 3B, 3F, 3H, and S3A–S3C). We previously reported that JNK signaling induced by aberrant cells drives apoptosis on either side of the clone interface, whereas a less-well-characterized pathway drives apoptosis in the clone interior.[4] This characteristic apoptotic pattern could be reproduced by Robo2-expressing clones (Figure 3I). Combined, we conclude that the expression of a single cell surface molecule, such as Robo2, is completely sufficient to induce all hallmarks of interface surveillance.

An important characteristic of interface surveillance is the strict position-dependent recognition of ectopic or missing fate-specifying pathways, which occurs in response to a pronounced mismatch in cell fate between clonal and neighboring cells. Accordingly, the endogenous Robo2-expression pattern should dictate where differences between clonal and neighboring cells are largest. Looking at the Robo2-expression pattern in third instar discs, we noticed that Robo2 is most highly expressed in the anterior notum and the hinge-hinge fold region, whereas medium levels of expression can be found along the dorsal-ventral boundary. In the dorsal and ventral pouch, Robo2 expression is low (Figure 3G). Therefore, we predicted that Robo2-expressing clones should elicit interface surveillance responses in the pouch but not the anterior notum, whereas Robo2-RNAi-expressing clones should elicit responses in the notum and not the pouch. Indeed, Robo2-expressing clones induced actin enrichment and JNK interface signaling in the pouch but not the notum, whereas Robo2-RNAi-expressing clones induced these responses in the notum but not the pouch (Figures 3B and 3C). The Robo2-GFP construct helped to visualize these spatially restricted JNK responses for Robo2-expressing and Robo2-RNAi-expressing clones with respect to the endogenous Robo2 expression pattern (Figures S3D and

markers Patched (Ptc, expressed in anterior cells at the anterior/posterior compartment boundary) and Wingless (Wg, expressed in cells on both sides of the dorsal/ventral compartment boundary) are shown in magenta and light magenta, respectively. All illustrated expression patterns were observed in $n \geq 4$ wing discs in $n \geq 2$ experimental replicates.

(B–D) Wing discs expressing fusion proteins from *robo2-GFP*, *eph-GFP*, and *ten-m-GFP* constructs under native regulatory control (gray or magenta). Ptc and Wg demarcate A/P and D/V compartment boundaries. Images are shown at same scale.

(B′–D′′) Pouch domains of *robo2-GFP*-, *eph-GFP*-, and *ten-m-GFP*-expressing wing discs (gray or cyan), also stained for the adherens junction marker E-cadherin (Ecad, gray or magenta) and cortical F-actin (by Phalloidin, gray or yellow). Apical (′) and lateral (′′) local-z-projections, displaying receptor localization relative to junctional Ecad and relative to more lateral domains. Images are shown at same scale. Please note that wing discs are not the same as in (B)–(D). Related to Figure S2.

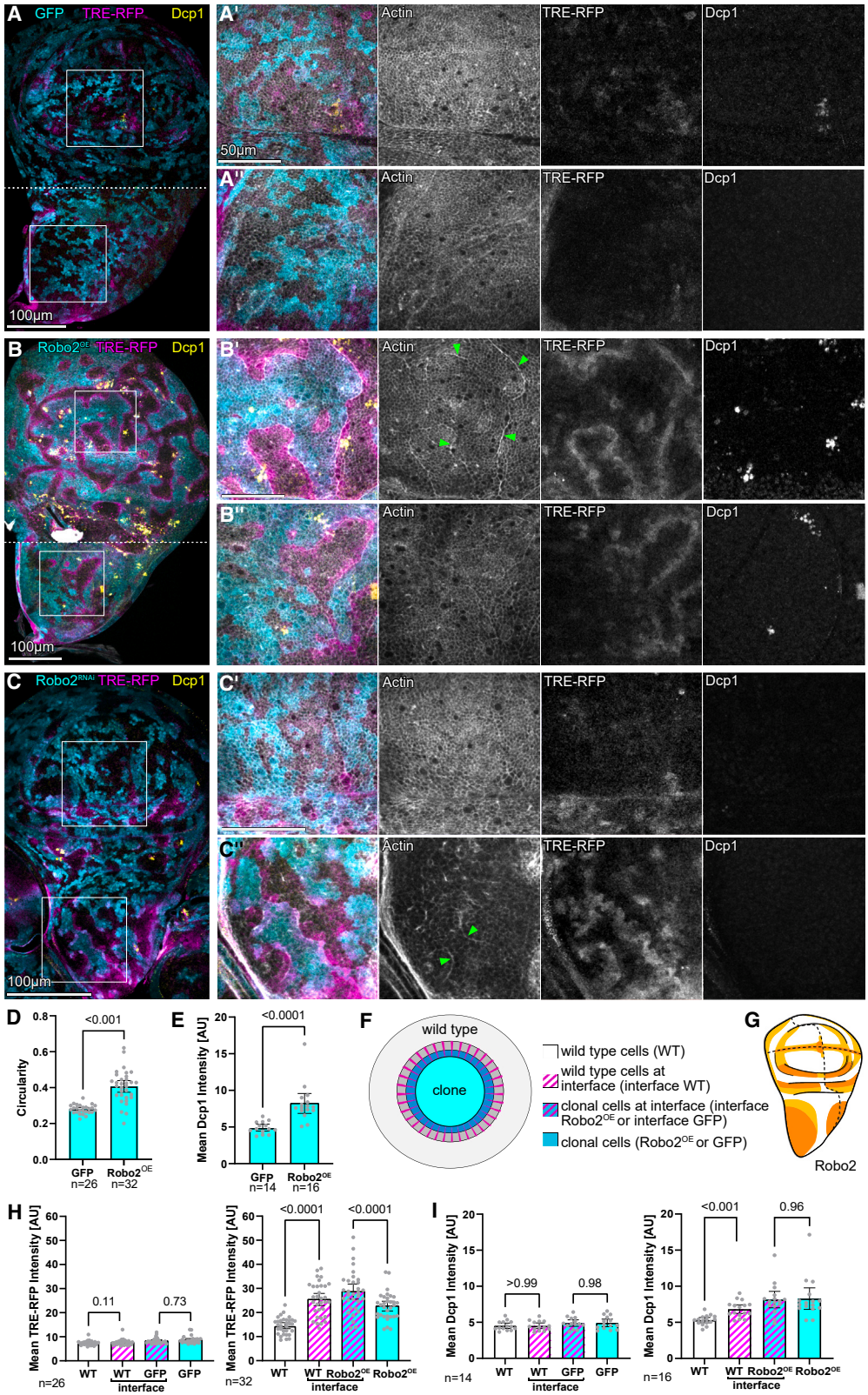

Figure 3. A mismatch of Robo2 receptor expression levels between neighboring cells is detected by interface surveillance

(A–C) Mosaic wing disc with wild-type clones expressing *UAS-GFP* (GFP, cyan) (A), and in addition, either *UAS-robo2* (Robo2^{OE}) (B) or *UAS-robo2-RNAi* (Robo2^{RNAi}) to reduce Robo2 function (C). TRE-RFP expression is reporting JNK pathway activity (gray or magenta). Antibody staining against the cleaved

(legend continued on next page)

S3E). These results demonstrate that cells, which create pronounced differences and thus a mismatch in Robo2 expression levels, are robustly detected by interface surveillance within the endogenous Robo2 expression pattern, suggesting that Robo2 may contribute to detection and removal of aberrant cells in a context-specific manner.

Robo2 and Robo3 mediate interface surveillance in a Slit-independent manner

Intrigued by the ability of Robo2 to induce interface surveillance, we next investigated the functional properties of the Robo2 receptor and the other Robo family members Robo1 and Robo3, as well as the known Robo-ligand Slit.

First, we wanted to test, whether in addition to actin, other cytoskeletal effectors were also recruited by Robo2-dependent interface surveillance. We therefore analyzed the localization of a GFP-tagged non-muscle myosin II regulatory light chain (Sqh-GFP) to visualize the actin motor myosin II, which enriches at the interface between wild-type and aberrant cells.[3] Moreover, we visualized Enabled (Ena), the *Drosophila* Ena/Vasp actin polymerase and an effector of Robo receptors in neuronal systems.[46] We also stained for phosphorylated tyrosine (pTyr), a marker of cellular interfaces between normal and oncogenic cells in mammalian epithelial tissue culture models.[47] We found that all markers enriched at interfaces of Robo2-expressing clones in the pouch (Figures 4A and 4B). However, as expected from the position-dependent recognition of clones, enrichment of Sqh-GFP, Ena, or pTyr was absent from interfaces of clones in the anterior notum (Figures 4C and 4D). These observations strongly indicate that Robo2 targets actomyosin regulation in epithelial tissues to mediate interface surveillance responses.

We next wanted to test if the downstream signal transduction by the Robo2 cytosolic domain is required for the induction of interface surveillance. To this end, we expressed a Robo2-construct that lacks the cytosolic domain (Robo2$^{\Delta cyto}$), preventing downstream signaling from the expressed Robo2 receptors. We find that Robo2$^{\Delta cyto}$-expressing clones also induced interface surveillance hallmarks, such as clone smoothening, actin enrichment, and JNK signaling at the interface (Figure 4E). Importantly, the presence of endogenous Robo2 in this genetic background only allows for the conclusion that cytosolic signaling by the overexpressed Robo2 is not required for induction of interface surveillance. We thus wanted to test the requirement of the well-characterized Robo-ligand Slit, which activates canonical receptor signaling. We expressed a Robo2-construct that lacks the extracellular immunoglobulin (Ig)-domains 1 and 2 (Robo2$^{\Delta Ig1+2}$) required for Slit ligand binding.[26,48–50] We find that Robo2$^{\Delta Ig1+2}$-expressing clones phenocopy the interface surveillance hallmarks of full-length Robo2-misexpression by displaying smoothening, actin enrichment, and JNK signaling at the interface (Figure 4F). This experiment demonstrates that the Slit-binding domain of Robo2 is not required for interface surveillance. To further provide support for this conclusion, we analyzed the function of Slit in wing imaginal disc. As reported before,[51] Slit is broadly expressed in imaginal discs (Figure S4A), but neither clonal overexpression of Slit or its downregulation using a validated RNAi construct induced JNK signaling at clonal interfaces (Figures 4G, 4H, and S4C). Similarly, Robo1, the Robo family member best described for Slit interaction, is broadly expressed in wing discs (Figure S4B). Yet, neither clonal overexpression nor downregulation of Robo1 using a validated RNAi induced JNK interface surveillance responses (Figures 4I, 4J, S4D, and S4E). Combined, these results suggest that Robo2 misexpression induces interface surveillance via a non-canonical Robo receptor activity and that classical Robo-Slit-mediated signaling may not be required.

Robo3 represents the third and last member of the Robo receptor family in flies. Interestingly, Robo3 shares a higher sequence similarity in extracellular and intracellular signaling domains with Robo2 than with Robo1.[52] We thus asked if Robo3-misexpression may also induce interface surveillance. In developing wing discs, Robo3 is expressed at barely detectable levels (Figure S5A). Hence, we reasoned that overexpression of Robo3 should strongly induce interface surveillance because Robo3-overexpressing clones would create pronounced differences in Robo3 levels to surrounding wild-type cells (Figure S5B). Indeed, Robo3-expressing clones induced clone smoothening, actin enrichment, JNK signaling, and apoptosis at clonal interfaces (Figures 5A and S5C). Moreover, Sqh-GFP, Ena, and pTyr were enriched at interfaces of Robo3-expressing clones (Figures S5D and S5E). In contrast, we did not observe any response when we expressed a validated Robo3-RNAi construct in mosaic clones (Figures 5B, S5F, and S5G). This result is consistent with a context-dependent model

effector caspase (Dcp1) visualizes apoptosis (gray or yellow). Phalloidin visualizes cortical F-actin (gray). Please note that JNK activity is physiologically elevated at the A/P compartment boundary in wing discs at this developmental stage. White frame marks region shown to the right in (A′), (B′), (C′ pouch), (A″), (B″), and (C″ notum). Please note the actin enrichment at the clone interface (green arrows in B″ and C′). The dotted line indicates stitching of confocal images with different z positions. Image sets are shown at the same scale.

(D and E) Graphs depicting circularity and apoptosis observed for individual *UAS-GFP*- (GFP) and *UAS-Robo2*- (Robo2^{OE}) expressing clones. Sample number (n) for individual wing discs and p values of a two-tailed, unpaired t test are displayed in graphs. Error bars represent mean and 95% confidence interval.

(F) Illustration of regions of interest (ROIs) relative to the clonal interface defined for quantitative image analysis (see also Figures S3A–S3C). There are non-labeled wild-type cells (white) or *UAS-GFP*-labeled clonal cells (cyan) in the wing disc. Clonal cells which additionally express *UAS-Robo2* are abbreviated as Robo2^{OE}. Both GFP-labeled (cyan) and non-labeled (white) cells are separated into cells, which are in contact with the other cell type at the interface (magenta stripes), and the remaining cells away from the interface.

(G) Illustration of the *robo2-GFP* expression pattern. Relative fluorescence intensity is depicted by the color intensity from low (white), medium (light orange) to high (dark orange).

(H and I) Graphs depicting mean fluorescence intensity of TRE-RFP reporter and mean Dcp1 intensity in the zones of measurement around clones, as depicted in Figure 3F. Graphs display results for mosaic discs with *UAS-GFP*-labeled clonal cells (left) or containing *UAS-Robo2* (Robo2^{OE})-expressing clones (right). Sample number (n) for individual wing discs and p values of a repeated measured one-way ANOVA with Tukey's multiple comparisons test are displayed in graphs. Error bars represent mean and 95% confidence interval.

Related to Figure S3 and Data S1.

CellPress
OPEN ACCESS

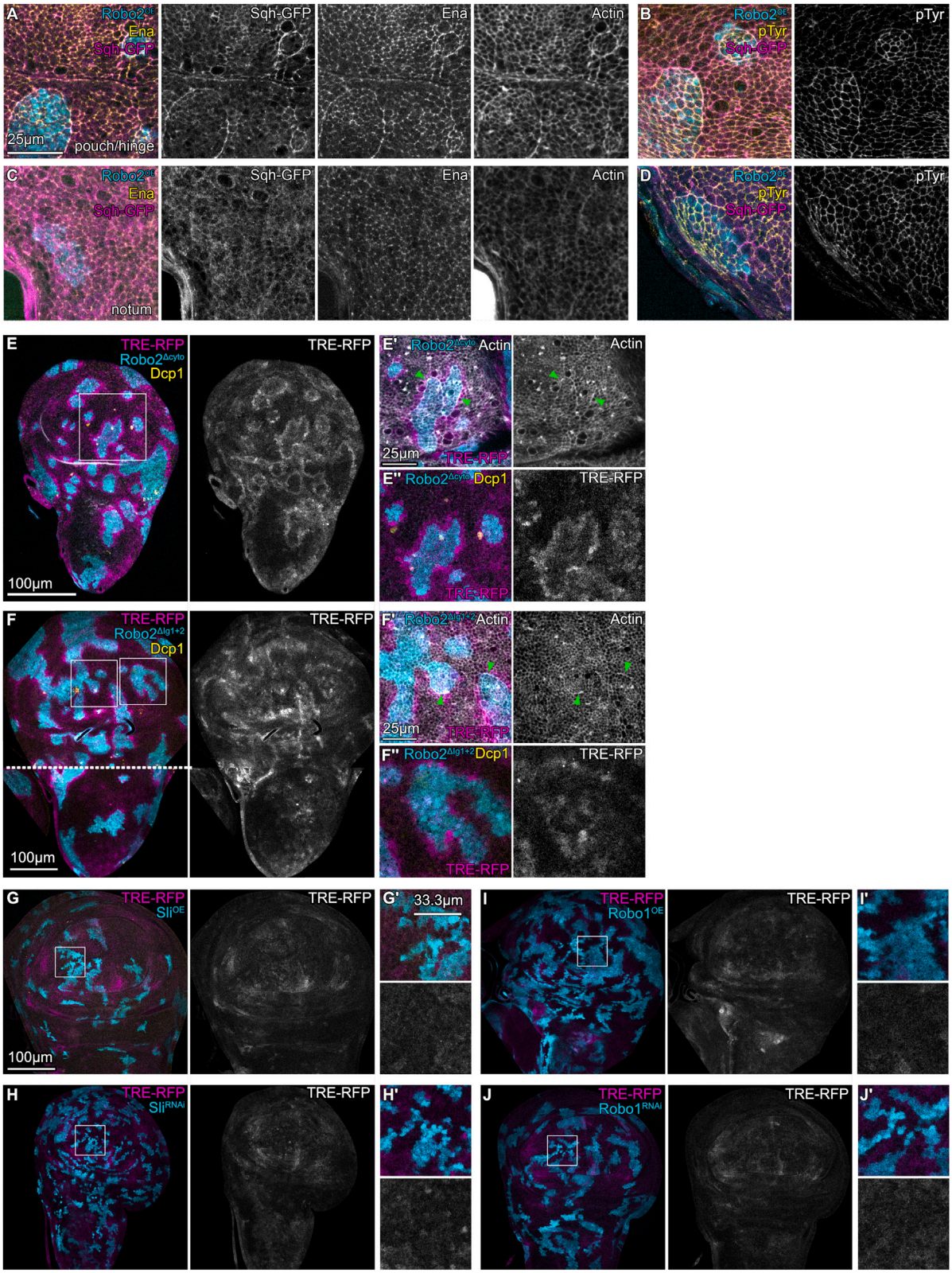

Figure 4. Robo2 induces interfaces surveillance independent of Slit and the receptor's cytosolic domain

(A–D) Mosaic wing disc with clones expressing *UAS-robo2* (Robo2^{OE}) (cyan) in either the pouch and hinge (A and B) or the notum region (C and D) of a wing disc. In (A) and (C) A GFP-tagged non-muscle myosin II regulatory light chain (Sqh-GFP) tracks the actin motor myosin II. antibody staining against Enabled (Ena)

(legend continued on next page)

of Robo3-dependent interface surveillance. Combined, we conclude that misexpression of either Robo2 or Robo3—with respect to levels in the surrounding wild-type cells—are completely sufficient to induce all hallmarks of interface surveillance.

One observation allowed us to further unravel the close functional relationship of Robo2 and Robo3 already suggested by previous studies in the developing nervous system.[53,54] Because Robo2 elicits interface surveillance depending on its endogenous pattern (Figures 5C–5E), we predicted that Robo3-expressing clones induce interfaces surveillance in the entire disc due to its ubiquitously low expression during development (Figure 5H). Contrary to those predictions, Robo3-misexpressing clones did not induce JNK signaling in the anterior notum, similar to Robo2-expressing clones (Figures 5F and 5G). We thus asked if Robo2 and Robo3 may act redundantly at clonal interfaces. To test this, we expressed Robo3 in Robo2-RNAi-expressing clones. We reasoned that if redundant, Robo3 expression will rescue the mismatch of Robo2 levels induced by Robo2-RNAi clones in the anterior notum. Strikingly, Robo3 expression robustly suppressed induction of JNK signaling and clone smoothening by Robo2-RNAi clones in the anterior notum (Figures 5I and 5J). Combined, our experiments demonstrate a pattern-specific function for Robo2 and Robo3 receptors in inducing interface surveillance and reveal that their high sequence similarity may cause functional redundancy, suggesting that both act through similar mechanisms in interface surveillance.

Expression of Robo receptors and interface surveillance molecules is regulated by fate-patterning pathways

If Robo2, Robo3, and other cell surface molecules identified in our genetic screen are really required to mediate the detection of aberrant and misspecified cells, then deregulation and genetic aberrations of fate-specifying pathways should alter expression levels of these proteins. Such upregulated or downregulated levels in aberrant cells would create pronounced expression level differences in cell surface molecules between neighboring cells, providing the basis for interface recognition.

To test this, we created clones misexpressing known cell-fate-specifying regulators: Thickveins (*tkv*^{RNAi}, *tkv*^{CA}), a Dpp/TGF-β-receptor important for wing disc patterning. Eyeless (*ey*), a Pax6 homolog and master regulator of the eye-specification network. Forkhead (*fkh*), a conserved transcription factor required for salivary gland specification. *ci*, the transcription factor activated by Hh signaling in the developing wing disc. Previous studies demonstrated that misexpression of these factors can drive dramatic respecification of cell fates and alterations of entire gene expression programs in imaginal discs.[55,56] We first tested if ectopic misspecification by these pathways affects Robo2 expression. Strikingly, expression levels of Robo2 were significantly altered, showing both upregulation and downregulation upon clonal misexpression of Tkv-RNAi, Fkh, or Ey in wing imaginal discs (Figures 6A–6D). Importantly, ectopic misspecification did not regulate Robo2 equally in every wing disc position. For instance, Ey increased expression levels of Robo2 in the pouch but not the notum, whereas Fkh downregulated Robo2 in the notum but not the pouch. The developing disc undergoes extensive patterning and different cell-type-specific signaling networks are active in the pouch, hinge, and notum cells. Therefore, our findings emphasize that the misexpression of one fate-specifying pathway is integrated into the intrinsic transcriptional network of different cell types, consistent with models of transcriptional networks in tissue patterning.[57,58] We thus suggest that—in response to ectopic deregulation of cell-fate-patterning pathways—the highly cell-type-specific transcriptional context determines whether to express a specific cell surface molecule or not.

Such reasoning predicts that changes to a single cell specification program may alter expression of several cell surface molecules simultaneously, including positive hits identified in our genetic screen. We thus wanted to understand how aberrant cell fate specification may reflect more complex changes to the composition of a cell surface code. We analyzed which cell surface molecules competent for interface surveillance are affected by deregulated Tkv signaling. Importantly, when we analyzed Tkv-misexpressing clones in the pouch, we found that they altered expression not just of Robo2 but also of Eph, Ten-m, Ten-a, and Tartan (Figures 6E–6N). Similarly, Fkh or Ci-expressing clones induced changes in expression of at least three cell surface molecules simultaneously (Figures S6A–S6I). These experiments strongly demonstrate that the alteration in activity of just one cell fate specification pathway causes changes in expression levels of multiple cell surface molecules. This alteration dramatically modifies the cell surface code of misspecified cells in comparison with surrounding wild-type cells.

To better understand how regulation of cell surface molecules may also be relevant for oncogenic processes driven by cell fate changes, we turned to the analysis of oncogenic mutations

visualizes localization of the *Drosophila* Ena/Vasp actin polymerase. Phalloidin visualizes cortical F-actin. In (B) and (D), antibody staining against phosphorylated tyrosine (pTyr) visualizes enhanced signaling activity at cellular junctions. Image sets are shown at the same scale. Projections of the apical junctional network were generated using the LocalZ-projector.

(E) Mosaic wing discs with clones (cyan) expressing *UAS-Robo2.DeltaC* (Robo2$^{\Delta cyto}$), a Robo2 construct lacking the cytosolic domains of the receptor. White frame marks the region shown in (E′) and (E″). Please note the actin enrichment at the clone interface (green arrows in E′).

(F) Mosaic wing discs with clones (cyan) expressing *UAS-Robo2.DeltaIg1+2* (Robo2 $^{\Delta Ig1+2}$), a Robo2 construct lacking the Ig1 and Ig2 domains of the extracellular part of the receptor. Please note that the Ig1 receptor domain has been shown to convey the binding of the Slit ligand. White frame marks region shown in (F′) and (F″). Please note the actin enrichment at the clone interface (green arrows in F′).

(G and H) Mosaic wing discs with clones (cyan) expressing either *UAS-sli.D* (Sli^{OE}) (G) or *UAS-sli-RNAi* (Sli^{RNAi}) (H). White frame marks the region shown in (G′) and (H′). Image sets are shown at the same scale.

(I and J) Mosaic wing discs with clones (cyan) expressing either *UAS-robo1* (Robo1^{OE}) (I) or *UAS-robo1-RNAi* (Robo1^{RNAi}) (J). White frame marks the region shown in (I′) and (J′). Image sets are shown at the same scale as (G) and (H).

TRE-RFP expression is reporting JNK pathway activity (gray or magenta). Antibody staining against the cleaved effector caspase (Dcp1) visualizes apoptosis (yellow). Phalloidin visualizes cortical F-actin (gray).

Related to Figure S4.

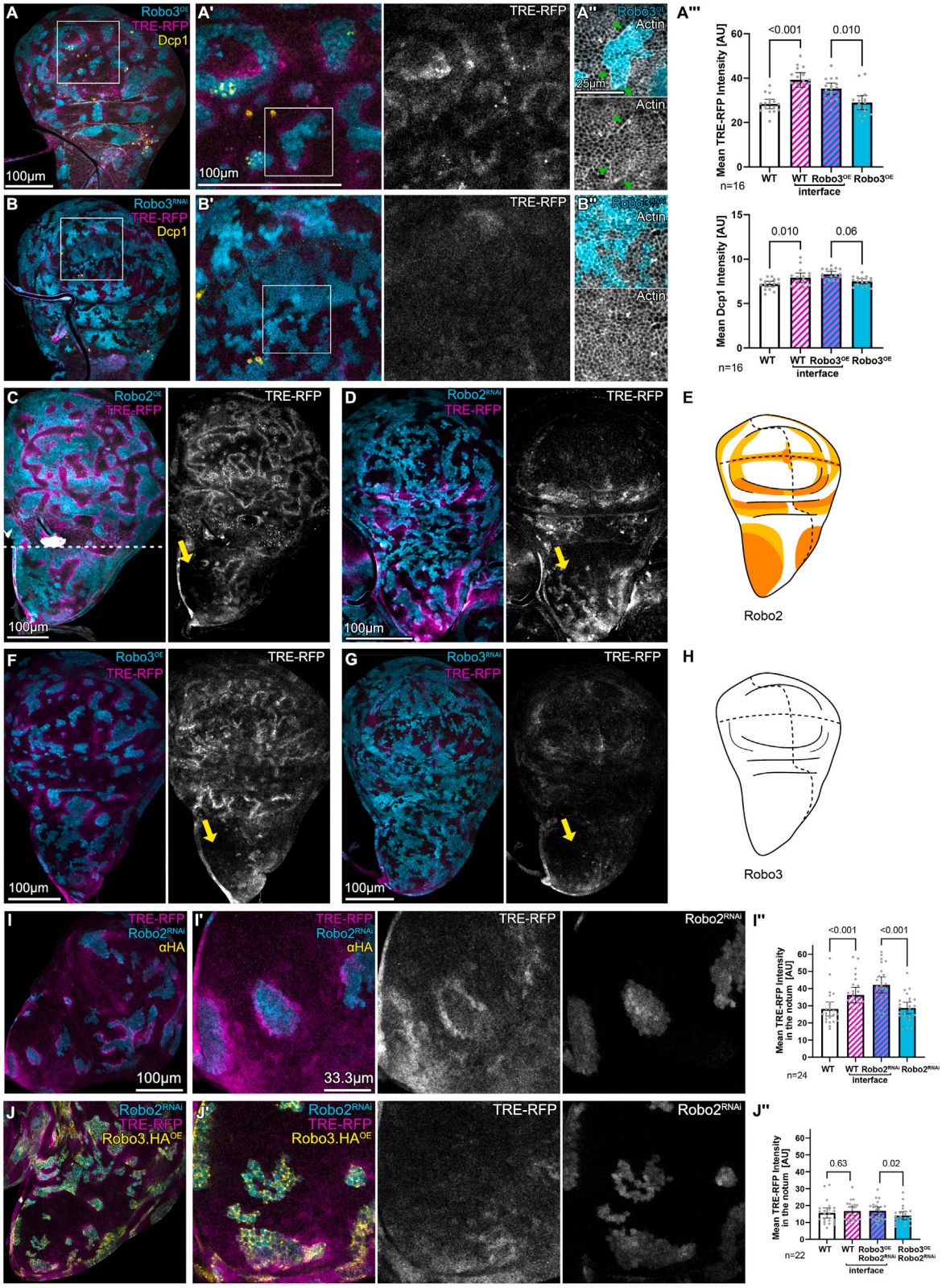

Figure 5. Robo3 induces interface surveillance and functions redundantly with Robo2

(A and B) Mosaic wing discs with clones (cyan) expressing either *UAS-robo3.HA* (Robo3^{OE}) (A) or *UAS-robo3-RNAi* (Robo3^{RNAi}) (B). TRE-RFP expression is reporting JNK pathway activity (gray or magenta in all panels). Antibody staining against the cleaved effector caspase (Dcp1) visualizes apoptosis (yellow).

(legend continued on next page)

incurred by Ras^{V12}. Ras signals through the EGF/ERK pathway and regulates both proliferation and wing fate patterning.[59] We previously reported that Ras^{V12}-expressing cells induce clone smoothening, actin enrichment, and JNK signaling at clonal interfaces (Figure S6J).[3,60] Yet, Ras^{V12} cells evade apoptosis, thereby allowing them to form slow-growing tumors.[4] To understand if Ras^{V12}-expressing cells may be initially detected by altered expression of cell surface markers, we monitored expression of cell surface molecules in Ras^{V12} mosaic discs. Indeed, Ras^{V12}-expressing clones deregulated expression of Robo2, Eph, Ten-m, and others (Figures 6O–6T and S6K–S6R). These observations provide further support for our conclusion that just a single fate-specifying aberration will alter the expression of multiple cell surface molecules and thereby drive complex changes in the cell surface code composition.

To understand whether expression of these cell surface molecules may also be utilized by other tissue-intrinsic error correction mechanisms, we analyzed genetic models of classical cell competition. In cell competition, the comparison of proteostatic or metabolic fitness between neighboring cells drives cell elimination, such that less fit "loser" cells are eliminated by fit "winner" cells.[61–68] Previous studies indicate that loser cells start to express a specific isoform of the cell surface molecule Flower, which marks them for elimination by winner cells in a cell-contact-dependent manner.[69,70] To test whether also a Robo2, Eph, or Ten-m-dependent cell surface code is associated with winner or loser cell state, we analyzed expression of these cell surface molecules in imaginal discs mosaic for a Myc-expressing winner genotype. In agreement with the model that cell competition and interface surveillance are mechanistically distinct error correction mechanisms, we found that Myc-expressing clones did not display pronounced alterations of cell surface receptor expression patterns that were predictive of either winner or loser fate (Figures 6U–6Z). Similarly, other genotypes linked to cell competition, tissue growth or cell survival, such as moderate activation or inhibition of Hippo/Warts signaling, did not alter cell surface molecule expression patterns (Figures S6U–S6AB). These observations demonstrate that a change in expression of the analyzed cell surface molecules is specific to cell-fate-specifying pathways and consequently highly correlates with activation of interface surveillance. This conclusion is strongly supported by our previous studies, in which cell competition and interface surveillance form distinct branches of tissue-intrinsic error correction and tumor suppression mechanisms that maintain the health of epithelial tissues.[4]

All our data presented so far provide strong genetic evidence that individual cell surface molecules are regulated by cell-fate-patterning pathways and that each is individually fully sufficient to induce interface surveillance. We now wanted to develop an approach to also provide evidence that deregulation of individual cell surface molecules is indeed genetically necessary for the detection of aberrant cells, even though we expected that genetically targeting a single molecule may not be sufficient to interfere with interface surveillance in response to changes in multiple cell surface molecules. Yet, we designed rescue experiments where we co-expressed a RNAi construct or overexpression construct for either Robo2, Eph, or Ten-m in clones with aberrant cell fates. We find that cells that aberrantly express *ey* and *fkh* still induced clone smoothening, enrichment of actin and even apoptosis, despite very targeted experiments to restore expression levels of Eph, Robo2, or Ten-m to that of surrounding cells (Figures S7A–S7C). Similarly, Ras^{V12} clones that ectopically induce expression of Eph or Robo2 in the peripheral pouch still activated interface surveillance responses despite targeted knockdown of Robo2 or Eph (Figures S7D and S7E). Yet, to really test whether equalizing expression levels of just one cell surface molecule between aberrant cells and surrounding cells can suppress interface surveillance, we expressed UAS-RNAi constructs for molecules that are upregulated in the peripheral pouch and hinge domain by tkv^{CA} (where Tkv is not normally active) under the control of *en*-GAL4. Thereby, all cells in the posterior compartment lacked either Eph or Ten-m at the time

Phalloidin visualizes cortical F-actin (gray). White frames in (A) and (B) mark the region shown in (A′) and (B′). White frames in (A′) and (B′) mark the regions shown in (A″) and (B″). Image sets are shown at the same scale. Please note the actin enrichment at clone interfaces in (A″) (green arrows). (A‴) Graphs depicting mean fluorescence intensity of TRE-RFP reporter and mean Dcp1 intensity in the zones of measurement around clones, as depicted in Figure 3F. Graphs display results for mosaic discs containing *UAS-Robo3.HA* ($Robo3^{OE}$)-expressing clones. See Figure S5C‴ for *UAS-GFP*-labeled clonal cells as wild-type control. Sample number (n) for individual wing discs and p values of a repeated measured one-way ANOVA with Tukey's multiple comparisons test are displayed in graphs. Error bars represent mean and 95% confidence interval.

(C and D) Mosaic wing discs where clones (cyan) express either *UAS-robo2* ($Robo2^{OE}$) (C) or express *UAS-robo2-RNAi* ($Robo2^{RNAi}$) (D). Yellow arrows indicate anterior notum region. TRE-RFP expression is reporting JNK pathway activity (gray or magenta). The dotted line indicates stitching of confocal images, with different z positions.

(E) Illustration of the *robo2-GFP* expression pattern. Relative fluorescence intensity is depicted by the color intensity from low (white), medium (light orange) to high (dark orange).

(F and G) Mosaic wing discs where clones (cyan) express either *UAS-robo3* ($Robo3^{OE}$) (F) or express *UAS-robo3-RNAi* ($Robo3^{RNAi}$) (G). Yellow arrows indicate anterior notum region. TRE-RFP expression is reporting JNK pathway activity (gray or magenta). Please note the absence of JNK activation in the notum region in (F), reminiscent of JNK activation by $Robo2^{OE}$ in (C).

(H) Illustration of the Robo3 expression in the wing disc as visualized by Robo3 antibodies. Please note that Robo3 is hardly expressed in the wing disc. See Figure S5A.

(I and J) Mosaic wing discs with clones expressing either *UAS-robo2-RNAi* ($Robo2^{RNAi}$) (I) or both *UAS-robo2-RNAi* ($Robo2^{RNAi}$) and *UAS-robo3.HA* ($Robo3.HA^{OE}$) (J). TRE-RFP expression is reporting JNK pathway activity (gray or magenta). Antibody staining against HA tag (αHA) visualizes the presence of the *UAS-robo3.HA* construct.

(I″ and J″) Graphs depicting the mean fluorescence intensity of TRE-RFP reporter in the zones of measurement around clones, as depicted in Figure 3F. Graphs display the results for mosaic discs containing *UAS-robo2-RNAi* ($Robo2^{RNAi}$) (I″), or both *UAS-robo2-RNAi* ($Robo2^{RNAi}$)- and *UAS-Robo3.HA* ($Robo3^{OE}$)-expressing clones. Sample number (n) for individual wing discs and p values of a repeated measured one-way ANOVA with Tukey's multiple comparisons test are displayed in graphs. Error bars represent mean and 95% confidence interval.

Related to Figure S5 and Data S2.

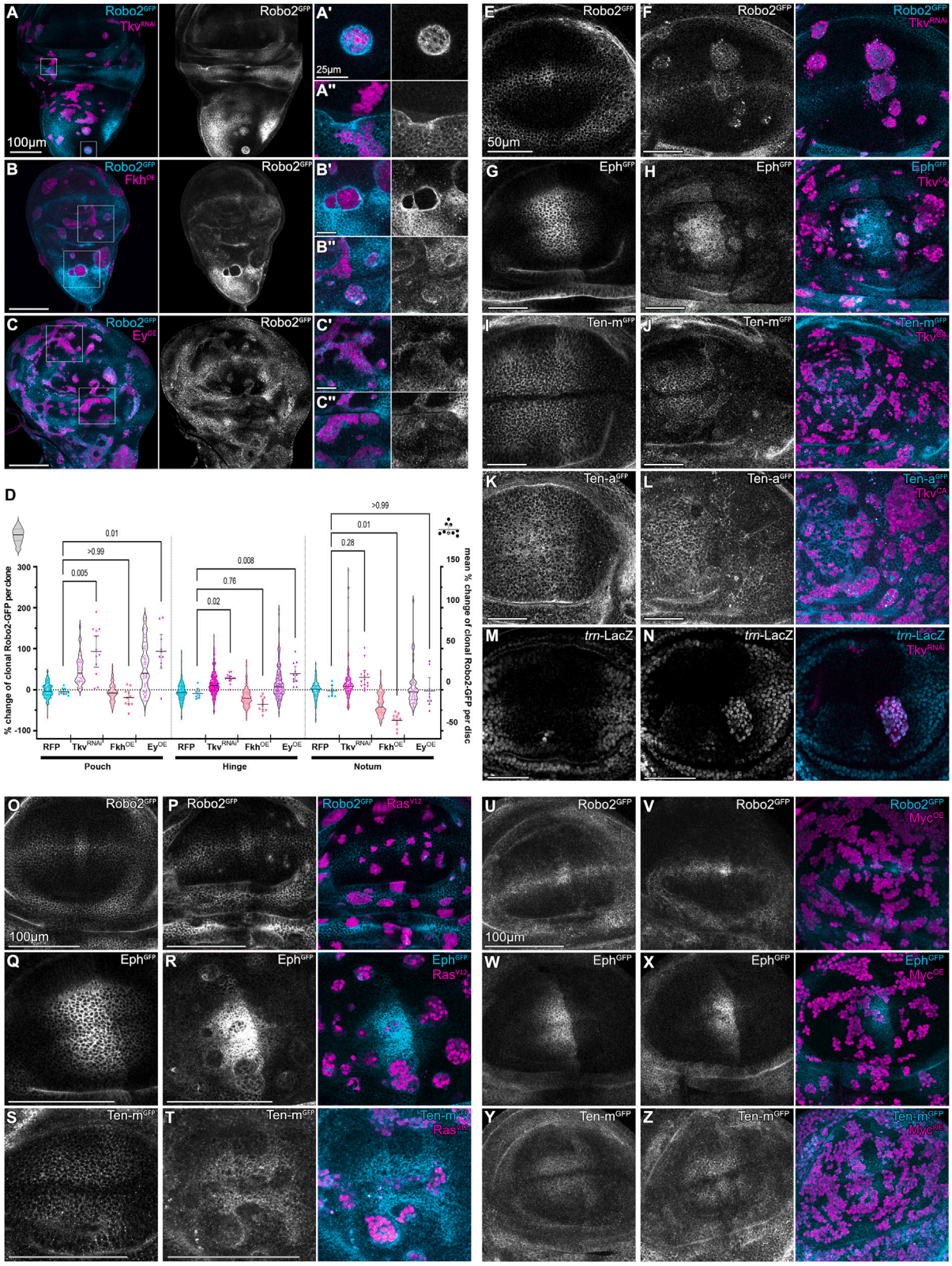

Figure 6. Expression of Robo receptors and other cell surface molecules is regulated by fate-patterning pathways

(A–C) Wing discs expressing *robo2-GFP* (Robo2^{GFP}) (gray or cyan). Mosaic clones (magenta) deregulate fate-specifying pathways by the expression of *UAS-tkv-RNAi* (Tkv^{RNAi}) (A), *UAS-fkh* (Fkh^{OE}) (B), or UAS-ey (Ey^{OE}) (C). White frames mark the regions shown in (A′)–(C″).

(legend continued on next page)

when we introduced *tkv*^{CA}-expressing clones using the LexA/LexO system.[71,72] However, removing either Eph or Ten-m from the surface code of posterior cells failed to affect interface surveillance responses of aberrant *tkv*^{CA}-expressing clones in the posterior pouch and hinge (Figures S7H–S7J).

These experiments, while challenging, support the multifactorial nature of a cell surface code, where multiple cell surface molecules are simultaneously deregulated upon cell fate misspecification, and deregulation of any one of them is sufficient to robustly induce interface surveillance. As a consequence, genetic experiments to analyze the necessity of individual molecules in the detection of aberrant cells are technically not possible, as our current genetic tools are incompatible with the possibly highly redundant nature of these molecules within the surface code. While we demonstrate that 12 proteins from our genetic screen are each sufficient to activate all hallmarks of interface surveillance, our study is thus limited by the lack of genetic evidence for the necessity of these molecules in mediating detection and recognition of aberrant cells in tissues.

DISCUSSION

Cell fate, cell surface code, and interface surveillance

In summary, we demonstrate that wing disc cells are equipped with various cell surface molecules, such as Robo2, Teneurin, or Eph. Almost all of them are expressed during development and deregulation of expression levels and the resulting expression level mismatch created at clonal interfaces is sufficient to induce all hallmarks of interface surveillance (Figure 7). Furthermore, aberrant cell fate programs deregulate expression of multiple cell surface molecules simultaneously. We propose that this reflects a physiological process of cell fate specification during development, in which cell fates establish a cell surface profile unique to each fate. Importantly, a single transcription factor does not always target the same cell surface molecule. Instead, the molecular composition is shaped by the cumulative activity of cell-type-specific transcriptional networks unique to each cell type. Finally, an altered surface code is a unique feature of cells experiencing cell fate deregulation and interface surveillance but not classical cell competition.

Among the protein families that we identified in our genetic screen, Eph/Ephrin, specifically, have previously been described to promote interface smoothening via actomyosin regulation in mosaic tissues and at compartment boundaries, both in *Drosophila* and mammalian systems.[36,43] Indeed, deregulation of Eph/Ephrin signaling induces actomyosin and Ena enrichment at clonal interfaces, clone smoothening and bilateral JNK signaling in our assays (Figures S7K–S7R). Similarly, Teneurins, or LRR proteins, such as Tartan, have been implicated in modulating actomyosin contractility or compartment boundary smoothening in different tissues. Moreover, regulation of their expression has been previously linked to fate specification in *Drosophila*.[36,37,44,73–77] Yet, we also describe a novel function of these molecules by implicating them in the induction of bilateral JNK activation. This suggests that these very different cell surface molecules may act not only through a shared set of cytoskeleton effectors but also through similar signaling effectors. The cell surface molecules identified in our screen are composed of very different structural motifs, including leucine-rich, Ig, YD, or cadherin repeats.[29,30,35,78] How these extracellular motifs or intracellular domains contribute to these shared effector modalities of actomyosin contractility and JNK signaling will be an important future avenue of our research.

Robo receptors in epithelia

Robo receptors are increasingly recognized to play a role in epithelia.[29] For example, recent molecular data from the mouse pancreas show that epithelial islet cells express Robo receptors. Disrupting Slit-Robo signaling disrupts embryonic islet formation and adult islet architecture.[79,80] In *Drosophila*, a JNK-Robo2-Ena axis is required for the elimination of *scrib* mutant cells in eye discs.[45] Importantly, we propose a distinct model for Robo2 and Robo3 receptors, where their mismatch at clonal boundaries is crucial rather than the mere presence of Robo2 receptors in aberrant cells. Moreover, JNK serves as a downstream effector of this mismatch, rather than an upstream regulator of Robo2 expression levels. In addition, neither the ligand Slit nor the cytosolic domain in Robo2 expression constructs are required for the induction of interface surveillance in our assays. In fact, ectopic levels of solely the extracellular domain of Robo2 are sufficient to activate interface signaling, suggesting that the extracellular domain of Robo2 may acts as interaction partner for cell surface molecules. Curiously, hRobo2 can interact in *trans* on neighboring cell surfaces, and the binding of LRR domains present in Slit result in conformation changes favoring the formation of an activating Robo2 dimer in *cis*.[50,81] Similarly, recent studies have focused on heterophilic receptor interactions involving Toll-like receptors containing LRR domains with Trn and Ten-m in *Drosophila* embryo patterning, receptors that we also find to induce interface surveillance.[44,82] Whether heterophilic interactions through LRR-domain proteins other than Slit play a role in Robo2-mediated interface surveillance remains to be investigated. Of note, we also find that Robo3 is capable of compensating for the loss of Robo2. Robo2 and Robo3 are

(D) Graph depicting the change of *robo2-GFP* in clonal cells at the interface expressing *UAS-RFP* (RFP), *UAS-tkv-RNAi* (Tkv^{RNAi}), *UAS-fkh* (Fkh^{OE}), or *UAS-ey* (Ey^{OE}) relative to the surrounding wild-type cells in the pouch, hinge, or notum region of the wing disc. Left axis shows the relative change for individual clones as depicted in the violin plots. Right axis shows the mean change of all the relative changes of individual clones per disc. n $\geq$ 7 wing discs per genotype are plotted, and p values of a Kruskal-Wallis test with Dunnett's multiple comparison test are displayed in the graph. Error bars represent mean and 95% confidence interval. (E, G, I, K, M, O, Q, S, U, W, and Y) Wing discs presenting the specific expression patterns of *robo2-GFP* (Robo2^{GFP}) (E, O, and U), *eph-GFP* (Eph^{GFP}) (G, Q, and W), *ten-m-GFP* (ten-m^{GFP}) (I, S, and Y), *ten-a-GFP* (Ten-a^{GFP}) (K), or *trn-LacZ* (*trn*-LacZ) (M) serving as a reference for the experimentally induced changes in (F), (H), (J), (L), (N), (P), (R), (T), (V), (X), and (Z).

(F, H, J, L, N, P, R, T, V, X, and Z) Wing discs expressing *robo2-GFP* (Robo2^{GFP}) (F,P,V), *eph-GFP* (Eph^{GFP}) (H, R, and X), *ten-m-GFP* (ten-m^{GFP}) (J, T, and Z), *ten-a-GFP* (Ten-a^{GFP}) (L), or *trn-LacZ* (*trn*-LacZ) (N) (gray or cyan) and carrying mosaic clones (magenta) with the knockdown of Tkv (Tkv^{RNAi}) (F and N), expression of a constitutively active Tkv (Tkv^{CA}) (H, J, and L), expression of *UAS-RasV12* (Ras^{V12}) (P, R, and T) or expression of Myc (Myc^{OE}) (V, X, and Z). Increasing Myc-levels creates super competitor cells, which will outcompete surrounding wild-type cells. Related to Figures S6 and S7 and Data S3 and S4.

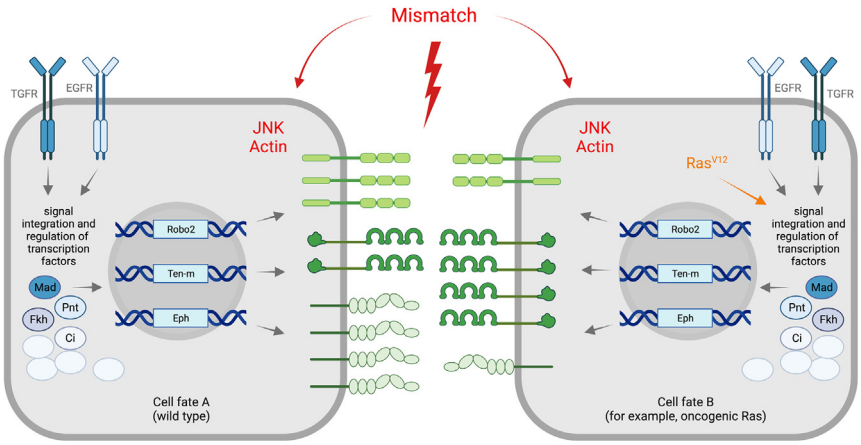

Figure 7. A mismatch in cell surface molecules induces interface surveillance

Signaling by different developmental patterning pathways (blue) is integrated in a cell-type-specific manner and a cell-type-specific set of transcription factors (blue) to drive the expression of a set of genes (blue) encoding for cell surface molecules (green), which are known to play a role in neuronal guidance and targeting. Thus, the combination of molecules displayed at the cell surface depends on the signal integration and fate specification at any position within the imaginal disc. Aberrant fate signals, for example, by the expression of oncogenic Ras^{V12} (orange), disrupt this cell-type-specific regulation of gene expression leading to a changed combination of cell surface molecules relative to that of the neighboring wild-type cell. The mismatch in cell surface molecules between neighboring cells induces all hallmarks of interface surveillance (red). Related to Figure S7.

closely related molecules with previously described functions in neuronal cell-cell recognition and differ from Robo1.[53,54] While all Robo receptors share similar extracellular domains, Robo2 and 3 retain only two of the four conserved cytoplasmic (CC) motifs found in Robo1 and lack the strongest Ena-recruiting CC-motif.[46] Interestingly, all Robo receptors retain a WAVE regulatory-complex-interacting receptor sequence (WIRS) through which actin regulation may be facilitated independent of Slit ligand binding.[83,84]

Regulation of neuronal cell surface molecules in cancer

Multiple recent studies revealed significant changes to the expression patterns of neuronal cell surface molecules in tumors, for example.[85,86] We demonstrate that Ras^{V12}-expressing cells disrupt the endogenous pattern of surface molecules, causing pronounced differences in the surface code and activation of interface surveillance responses. In mammalian epithelia, cells with oncogenic Ras signaling are detected and eliminated by a process termed epithelial defense against cancer (EDAC) akin to interface surveillance.[4,87,88] Eph/Ephrin signaling was shown to regulate the interaction of oncogenic Ras^{V12}-expressing cells with neighboring wild-type cells in cultured MDCK monolayers and pancreas *in vivo*.[89,90] Here, Ras^{V12}-expression induces EphA2 which underlies actin enrichment and cell shape changes upon interaction of wild-type and Ras^{V12}-expressing cells. This supports a model where interface surveillance mediated by altered expression of cell surface molecules may have important roles in tumor suppression by regulating the interaction between wild-type and aberrant cells. However, this very machinery can also promote tumor progression by triggering signaling pathways and actomyosin dynamics at the interface with wild-type cells. Aberrant cells may exhibit resistance to apoptosis, as exemplified by the case of Ras^{V12}-expressing cells, which would channel activation of JNK signaling and actomyosin dynamics toward migratory behaviors.[4]

Interface surveillance in development

Interface surveillance shares striking similarities with compartment boundary formation in developing tissues, where two cell populations of distinct fate mechanically segregate via the formation of a contractile actomyosin interface between them. Indeed, many of the molecules identified in our genetic screen facilitate actomyosin regulation during compartment boundary formation in vertebrate and invertebrate species.[24–26,36,37] The similarities between developmental morphogenesis and tissue-intrinsic error correction, relying on the same principle of receptor-mediated recognition and actomyosin driven segregation of cell populations, point toward a common evolutionary origin of the surface code subsequently adapted for developmental and homeostatic processes. In fact, cellular function of neuronal axon guidance in neuronal tissues may have originally evolved in evolutionarily more ancient epithelia. Ultimately, the cell surface code formed by so-called neuronal axon guidance molecules and related factors may represent an ancient system to distinguish self from non-self in physiological and pathological contexts.

STAR★METHODS

Detailed methods are provided in the online version of this paper and include the following:

- KEY RESOURCES TABLE
- RESOURCE AVAILABILITY
  - Lead contact
  - Materials availability
  - Data and code availability
- EXPERIMENTAL MODEL
- METHOD DETAILS
  - Drosophila genetics
  - Immunohistochemistry
  - Image acquisition and image display
  - Illustration of expression patterns
- IMAGE QUANTIFICATION AND STATISTICAL ANALYSIS
  - Region of interest (ROI) segmentation and quantification workflow

SUPPLEMENTAL INFORMATION

Supplemental information can be found online at https://doi.org/10.1016/j.cub.2024.01.053.

ACKNOWLEDGMENTS

We thank the staff of the Life Imaging Center (LIC) in the Hilde Mangold House (HMH) of the University of Freiburg for help with their confocal microscopy resources and the excellent support in image recording. We specifically thank the DFG for supporting our imaging work through project number 414136422. We thank Timothy Evans, David Bilder, Ishwar Hariharan, George Pyrowolakis, Martin Juenger, Suzanne Eaton, Dirk Bohmann, Mirka Uhlirova, Helena Richardson, Jennifer Zallen, Ruth Johnson, Frank Schnorrer, David Strutt, Andrea Brand, Yoshimasa Yagi, Karl-Friederich Fischbach, and Mel Feany for sharing reagents. We thank the Bloomington Drosophila Stock Centre (BDSC), the Vienna Drosophila Stock Collection (VDRC) and the Developmental Studies Hybridoma Bank (DSHB), and the Monoclonal Antibody Core Facility at the Helmholtz Zentrum Munich for providing fly stocks and antibodies. We also thank the SGBM and IMPRS-IE graduate schools for supporting our doctoral researchers. Funding for this work was provided by the Deutsche Forschungsgemeinschaft (DFG, German Research Foundation) under Germany s Excellence Strategy (CIBSS—EXC-2189—project ID 390939984 and GSC-4, Spemann Graduate School of Biology and Medicine), the CRC 850 (Control of Cell Motility in Development and Cancer), the Heisenberg Program (CL490/3-1), the Boehringer Ingelheim Foundation Plus3 and RiseUp! Programmes, and the International Max Planck Research School for Immunobiology, Epigenetics, and Metabolism (Max Planck Institute of Immunobiology and Epigenetics, Freiburg).

AUTHOR CONTRIBUTIONS

Conceptualization, F.F., A.F., and A.-K.C.; data curation, F.F., L.E., A.F., and K.H.; formal analysis, F.F., A.F., L.E., and V.W.; funding acquisition, A.-K.C.; investigation, F.F., A.F., L.E., K.H., D.P., V.W., and R.B.; methodology, F.F., A.F., L.E., K.H., D.P., V.W., and R.B.; project administration, A.-K.C.; supervision, A.-K.C.; validation, F.F., A.F., L.E., K.H., D.P., V.W., and R.B.; visualization, F.F., L.E., and A.F.; writing – original draft, F.F. and A.-K.C.; writing – review & editing, L.E., A.F., F.F., and A.-K.C.

DECLARATION OF INTERESTS

The authors declare no competing interests.

Received: March 9, 2023
Revised: September 29, 2023
Accepted: January 19, 2024
Published: February 12, 2024

REFERENCES

1. Starostik, M.R., Sosina, O.A., and McCoy, R.C. (2020). Single-cell analysis of human embryos reveals diverse patterns of aneuploidy and mosaicism. Genome Res. *30*, 814–825.
2. Martincorena, I. (2019). Somatic mutation and clonal expansions in human tissues. Genome Med. *11*, 35.
3. Bielmeier, C., Alt, S., Weichselberger, V., La Fortezza, M., Harz, H., Jülicher, F., Salbreux, G., and Classen, A.K. (2016). Interface Contractility between Differently Fated Cells Drives Cell Elimination and Cyst Formation. Curr. Biol. *26*, 563–574.
4. Prasad, D., Illek, K., Fischer, F., Holstein, K., and Classen, A.K. (2023). Bilateral JNK activation is a hallmark of interface surveillance and promotes elimination of aberrant cells. eLife *12*.
5. Gibson, M.C., and Perrimon, N. (2005). Extrusion and death of DPP/BMP-compromised epithelial cells in the developing Drosophila wing. Science *307*, 1785–1789. 307/5716/1785.
6. Shen, J., and Dahmann, C. (2005). Extrusion of cells with inappropriate Dpp signaling from Drosophila wing disc epithelia. Science *307*, 1789–1790.
7. Widmann, T.J., and Dahmann, C. (2009). Wingless signaling and the control of cell shape in Drosophila wing imaginal discs. Dev. Biol. *334*, 161–173. S0012-1606(09)01063-X.
8. Widmann, T.J., and Dahmann, C. (2009). Dpp signaling promotes the cuboidal-to-columnar shape transition of Drosophila wing disc epithelia by regulating Rho1. J. Cell Sci. *122*, 1362–1373.
9. Pallavi, S.K., Ho, D.M., Hicks, C., Miele, L., and Artavanis-Tsakonas, S. (2012). Notch and Mef2 synergize to promote proliferation and metastasis through JNK signal activation in Drosophila. EMBO J. *31*, 2895–2907.
10. Gandille, P., Narbonne-Reveau, K., Boissonneau, E., Randsholt, N., Busson, D., and Pret, A.M. (2010). Mutations in the polycomb group gene polyhomeotic lead to epithelial instability in both the ovary and wing imaginal disc in Drosophila. PLoS One *5*, e13946.
11. Bessa, J., Carmona, L., and Casares, F. (2009). Zinc-finger paralogues tsh and tio are functionally equivalent during imaginal development in Drosophila and maintain their expression levels through auto- and cross-negative feedback loops. Dev. Dyn. *238*, 19–28.
12. Aldaz, S., Morata, G., and Azpiazu, N. (2005). Patterning function of homothorax/extradenticle in the thorax of Drosophila. Development *132*, 439–446.
13. Beuchle, D., Struhl, G., and Müller, J. (2001). Polycomb group proteins and heritable silencing of Drosophila Hox genes. Development *128*, 993–1004.
14. Prober, D.A., and Edgar, B.A. (2000). Ras1 promotes cellular growth in the Drosophila wing. Cell *100*, 435–446.
15. Liu, X., Grammont, M., and Irvine, K.D. (2000). Roles for scalloped and vestigial in regulating cell affinity and interactions between the wing blade and the wing hinge. Dev. Biol. *228*, 287–303.
16. Worley, M.I., Setiawan, L., and Hariharan, I.K. (2013). TIE-DYE: a combinatorial marking system to visualize and genetically manipulate clones during development in Drosophila melanogaster. Development *140*, 3275–3284.
17. Perea, D., Molohon, K., Edwards, K., and Díaz-Benjumea, F.J. (2013). Multiple roles of the gene zinc finger homeodomain-2 in the development of the Drosophila wing. Mech. Dev. *130*, 467–481.
18. Gold, K.S., and Brand, A.H. (2014). Optix defines a neuroepithelial compartment in the optic lobe of the Drosophila brain. Neural Dev. *9*, 18.
19. Classen, A.K., Bunker, B.D., Harvey, K.F., Vaccari, T., and Bilder, D. (2009). A tumor suppressor activity of Drosophila Polycomb genes mediated by JAK-STAT signaling. Nat. Genet. *41*, 1150–1155.
20. Bell, G.P., and Thompson, B.J. (2014). Colorectal cancer progression: lessons from Drosophila? Semin. Cell Dev. Biol. *28*, 70–77.
21. Organista, M.F., and De Celis, J.F. (2013). The Spalt transcription factors regulate cell proliferation, survival and epithelial integrity downstream of the Decapentaplegic signalling pathway. Biol. Open *2*, 37–48.
22. Villa-Cuesta, E., González-Pérez, E., and Modolell, J. (2007). Apposition of iroquois expressing and non-expressing cells leads to cell sorting and fold formation in the Drosophila imaginal wing disc. BMC Dev. Biol. *7*, 106.
23. Shen, J., Dahmann, C., and Pflugfelder, G.O. (2010). Spatial discontinuity of optomotor-blind expression in the Drosophila wing imaginal disc disrupts epithelial architecture and promotes cell sorting. BMC Dev. Biol. *10*, 23.
24. Sharrock, T.E., and Sanson, B. (2020). Cell sorting and morphogenesis in early Drosophila embryos. Semin. Cell Dev. Biol. *107*, 147–160.
25. Wang, J., and Dahmann, C. (2020). Establishing compartment boundaries in Drosophila wing imaginal discs: An interplay between selector genes, signaling pathways and cell mechanics. Semin. Cell Dev. Biol. *107*, 161–169.
26. Addison, M., and Wilkinson, D.G. (2016). Segment Identity and Cell Segregation in the Vertebrate Hindbrain. Curr. Top. Dev. Biol. *117*, 581–596.
27. Tsai, T.Y., Garner, R.M., and Megason, S.G. (2022). Adhesion-Based Self-Organization in Tissue Patterning. Annu. Rev. Cell Dev. Biol. *38*, 349–374.
28. Kania, A., and Klein, R. (2016). Mechanisms of ephrin-Eph signalling in development, physiology and disease. Nat. Rev. Mol. Cell Biol. *17*, 240–256.

29. Beamish, I.V., Hinck, L., and Kennedy, T.E. (2018). Making Connections: Guidance Cues and Receptors at Nonneural Cell-Cell Junctions. Cold Spring Harb. Perspect. Biol. *10*, a029165.

30. Moreland, T., and Poulain, F.E. (2022). To Stick or Not to Stick: The Multiple Roles of Cell Adhesion Molecules in Neural Circuit Assembly. Front. Neurosci. *16*, 889155.

31. Cortés, E., Pak, J.S., and Özkan, E. (2023). Structure and evolution of neuronal wiring receptors and ligands. Dev. Dyn. *252*, 27–60.

32. Zang, Y., Chaudhari, K., and Bashaw, G.J. (2021). New insights into the molecular mechanisms of axon guidance receptor regulation and signaling. Curr. Top. Dev. Biol. *142*, 147–196.

33. Klein, R., and Pasterkamp, R.J. (2021). Recent advances in inter-cellular interactions during neural circuit assembly. Curr. Opin. Neurobiol. *69*, 25–32.

34. Del Toro, D., Carrasquero-Ordaz, M.A., Chu, A., Ruff, T., Shahin, M., Jackson, V.A., Chavent, M., Berbeira-Santana, M., Seyit-Bremer, G., Brignani, S., et al. (2020). Structural Basis of Teneurin-Latrophilin Interaction in Repulsive Guidance of Migrating Neurons. Cell *180*, 323–339.e19.

35. Honig, B., and Shapiro, L. (2020). Adhesion Protein Structure, Molecular Affinities, and Principles of Cell-Cell Recognition. Cell *181*, 520–535.

36. Umetsu, D., Dunst, S., and Dahmann, C. (2014). An RNA interference screen for genes required to shape the anteroposterior compartment boundary in Drosophila identifies the Eph receptor. PLoS One *9*, e114340.

37. Paré, A.C., Naik, P., Shi, J., Mirman, Z., Palmquist, K.H., and Zallen, J.A. (2019). An LRR Receptor-Teneurin System Directs Planar Polarity at Compartment Boundaries. Dev. Cell *51*, 208–221.e6.

38. Chatterjee, N., and Bohmann, D. (2012). A versatile PhiC31 based reporter system for measuring AP-1 and Nrf2 signaling in Drosophila and in tissue culture. PLoS One *7*, e34063.

39. del Valle Rodríguez, A., Didiano, D., and Desplan, C. (2011). Power tools for gene expression and clonal analysis in Drosophila. Nat. Methods *9*, 47–55.

40. Sarov, M., Barz, C., Jambor, H., Hein, M.Y., Schmied, C., Suchold, D., Stender, B., Janosch, S., K J, V.V., Krishnan, R.T., et al. (2016). A genome-wide resource for the analysis of protein localisation in Drosophila. eLife *5*, e12068.

41. Venken, K.J.T., Schulze, K.L., Haelterman, N.A., Pan, H., He, Y., Evans-Holm, M., Carlson, J.W., Levis, R.W., Spradling, A.C., Hoskins, R.A., et al. (2011). MiMIC: a highly versatile transposon insertion resource for engineering Drosophila melanogaster genes. Nat. Methods *8*, 737–743.

42. Held, L.I., Jr. (2002). Imaginal Discs: the Genetic and Cellular Logic of Pattern Formation (Cambridge University Press).

43. Calzolari, S., Terriente, J., and Pujades, C. (2014). Cell segregation in the vertebrate hindbrain relies on actomyosin cables located at the interhombomeric boundaries. EMBO J. *33*, 686–701.

44. Lavalou, J., Mao, Q., Harmansa, S., Kerridge, S., Lellouch, A.C., Philippe, J.M., Audebert, S., Camoin, L., and Lecuit, T. (2021). Formation of polarized contractile interfaces by self-organized Toll-8/Cirl GPCR asymmetry. Dev. Cell *56*, 1574–1588.e7.

45. Vaughen, J., and Igaki, T. (2016). Slit-Robo Repulsive Signaling Extrudes Tumorigenic Cells from Epithelia. Dev. Cell *39*, 683–695.

46. Bashaw, G.J., Kidd, T., Murray, D., Pawson, T., and Goodman, C.S. (2000). Repulsive axon guidance: Abelson and Enabled play opposing roles downstream of the roundabout receptor. Cell *101*, 703–715.

47. Kajita, M., Sugimura, K., Ohoka, A., Burden, J., Suganuma, H., Ikegawa, M., Shimada, T., Kitamura, T., Shindoh, M., Ishikawa, S., et al. (2014). Filamin acts as a key regulator in epithelial defence against transformed cells. Nat. Commun. *5*, 4428.

48. Howard, L.J., Reichert, M.C., and Evans, T.A. (2021). The Slit-binding Ig1 domain is required for multiple axon guidance activities of Drosophila Robo2. Genesis *59*, e23443.

49. Fukuhara, N., Howitt, J.A., Hussain, S.A., and Hohenester, E. (2008). Structural and functional analysis of slit and heparin binding to immunoglobulin-like domains 1 and 2 of Drosophila Robo. J. Biol. Chem. *283*, 16226–16234.

50. Barak, R., Yom-Tov, G., Guez-Haddad, J., Gasri-Plotnitsky, L., Maimon, R., Cohen-Berkman, M., McCarthy, A.A., Perlson, E., Henis-Korenblit, S., Isupov, M.N., et al. (2019). Structural Principles in Robo Activation and Auto-inhibition. Cell *177*, 272–285.e16.

51. Sasse, S., and Klämbt, C. (2016). Repulsive Epithelial Cues Direct Glial Migration along the Nerve. Dev. Cell *39*, 696–707.

52. Simpson, J.H., Kidd, T., Bland, K.S., and Goodman, C.S. (2000). Short-Range and Long-Range Guidance by Slit and Its Robo Receptors: Robo and Robo2 Play Distinct Roles in Midline Guidance. Neuron *28*, 753–766.

53. Pappu, K.S., Morey, M., Nern, A., Spitzweck, B., Dickson, B.J., and Zipursky, S.L. (2011). Robo-3–mediated repulsive interactions guide R8 axons during Drosophila visual system development. Proc. Natl. Acad. Sci. USA *108*, 7571–7576.

54. Rajagopalan, S., Vivancos, V., Nicolas, E., and Dickson, B.J. (2000). Selecting a longitudinal pathway: Robo receptors specify the lateral position of axons in the Drosophila CNS. Cell *103*, 1033–1045.

55. Halder, G., Callaerts, P., and Gehring, W.J. (1995). Induction of ectopic eyes by targeted expression of the eyeless gene in Drosophila. Science *267*, 1788–1792.

56. Zecca, M., Basler, K., and Struhl, G. (1995). Sequential organizing activities of engrailed, hedgehog and decapentaplegic in the Drosophila wing. Development *121*, 2265–2278.

57. Beira, J.V., and Paro, R. (2016). The legacy of Drosophila imaginal discs. Chromosoma *125*, 573–592.

58. Ruiz-Losada, M., Blom-Dahl, D., Córdoba, S., and Estella, C. (2018). Specification and Patterning of Drosophila Appendages. J. Dev. Biol. *6*, 17.

59. De Celis, J.F. (2003). Pattern formation in the Drosophila wing: The development of the veins. BioEssays *25*, 443–451.

60. Prasad, D., Illek, K., Fischer, F., Holstein, K., and Classen, A.-K. (2022). Bilateral JNK activation is a hallmark of interface contractility and promotes elimination of aberrant cells. https://doi.org/10.1101/2022.06.20.496791.

61. Baumgartner, M.E., Dinan, M.P., Langton, P.F., Kucinski, I., and Piddini, E. (2021). Proteotoxic stress is a driver of the loser status and cell competition. Nat. Cell Biol. *23*, 136–146.

62. Blanco, J., Cooper, J.C., and Baker, N.E. (2020). Roles of C/EBP class bZip proteins in the growth and cell competition of Rp ('Minute') mutants in Drosophila. eLife *9*, e50535.

63. Ji, Z., Kiparaki, M., Folgado, V., Kumar, A., Blanco, J., Rimesso, G., Chuen, J., Liu, Y., Zheng, D., and Baker, N.E. (2019). Drosophila RpS12 controls translation, growth, and cell competition through Xrp1. PLoS Genet. *15*, e1008513.

64. Baker, N.E., Kiparaki, M., and Khan, C. (2019). A potential link between p53, cell competition and ribosomopathy in mammals and in Drosophila. Dev. Biol. *446*, 17–19.

65. Lee, C.H., Kiparaki, M., Blanco, J., Folgado, V., Ji, Z., Kumar, A., Rimesso, G., and Baker, N.E. (2018). A Regulatory Response to Ribosomal Protein Mutations Controls Translation, Growth, and Cell Competition. Dev. Cell *46*, 456–469.e4.

66. Baillon, L., Germani, F., Rockel, C., Hilchenbach, J., and Basler, K. (2018). Xrp1 is a transcription factor required for cell competition-driven elimination of loser cells. Sci. Rep. *8*, 17712.

67. Kale, A., Ji, Z., Kiparaki, M., Blanco, J., Rimesso, G., Flibotte, S., and Baker, N.E. (2018). Ribosomal Protein S12e Has a Distinct Function in Cell Competition. Dev. Cell *44*, 42–55.e4.

68. Ochi, N., Nakamura, M., Nagata, R., Wakasa, N., Nakano, R., and Igaki, T. (2021). Cell competition is driven by Xrp1-mediated phosphorylation of eukaryotic initiation factor 2alpha. PLoS Genet. *17*, e1009958.

69. Madan, E., Pelham, C.J., Nagane, M., Parker, T.M., Canas-Marques, R., Fazio, K., Shaik, K., Yuan, Y., Henriques, V., Galzerano, A., et al. (2019).

Flower isoforms promote competitive growth in cancer. Nature *572*, 260–264.

70. Rhiner, C., López-Gay, J.M., Soldini, D., Casas-Tinto, S., Martín, F.A., Lombardía, L., and Moreno, E. (2010). Flower forms an extracellular code that reveals the fitness of a cell to its neighbors in Drosophila. Dev. Cell *18*, 985–998.
71. Bosch, J.A., Tran, N.H., and Hariharan, I.K. (2015). CoinFLP: a system for efficient mosaic screening and for visualizing clonal boundaries in Drosophila. Development *142*, 597–606.
72. Yagi, R., Mayer, F., and Basler, K. (2010). Refined LexA transactivators and their use in combination with the Drosophila Gal4 system. Proc. Natl. Acad. Sci. USA *107*, 16166–16171.
73. Milán, M., Weihe, U., Pérez, L., and Cohen, S.M. (2001). The LRR proteins capricious and Tartan mediate cell interactions during DV boundary formation in the Drosophila wing. Cell *106*, 785–794.
74. Milán, M., Pérez, L., and Cohen, S.M. (2005). Boundary formation in the Drosophila wing: functional dissection of Capricious and Tartan. Dev. Dyn. *233*, 804–810.
75. Willecke, M., Hamaratoglu, F., Sansores-Garcia, L., Tao, C., and Halder, G. (2008). Boundaries of Dachsous Cadherin activity modulate the Hippo signaling pathway to induce cell proliferation. Proc. Natl. Acad. Sci. USA *105*, 14897–14902.
76. Bosveld, F., Guirao, B., Wang, Z., Rivière, M., Bonnet, I., Graner, F., and Bellaïche, Y. (2016). Modulation of junction tension by tumor suppressors and proto-oncogenes regulates cell-cell contacts. Development *143*, 623–634.
77. Milán, M., Pérez, L., and Cohen, S.M. (2002). Short-range cell interactions and cell survival in the Drosophila wing. Dev. Cell *2*, 797–805.
78. Fulford, A.D., and McNeill, H. (2020). Fat/Dachsous family cadherins in cell and tissue organisation. Curr. Opin. Cell Biol. *62*, 96–103.
79. Gilbert, J.M., Adams, M.T., Sharon, N., Jayaraaman, H., and Blum, B. (2021). Morphogenesis of the Islets of Langerhans Is Guided by Extraendocrine Slit2 and Slit3 Signals. Mol. Cell. Biol. *41*, e0045120.
80. Waters, B.J., and Blum, B. (2022). Axon Guidance Molecules in the Islets of Langerhans. Front. Endocrinol. *13*, 869780.
81. Evans, T.A., Santiago, C., Arbeille, E., and Bashaw, G.J. (2015). Robo2 acts in trans to inhibit Slit-Robo1 repulsion in pre-crossing commissural axons. eLife *4*, e08407.
82. Paré, A.C., Vichas, A., Fincher, C.T., Mirman, Z., Farrell, D.L., Mainieri, A., and Zallen, J.A. (2014). A positional Toll receptor code directs convergent extension in Drosophila. Nature *515*, 523–527.
83. Chaudhari, K., Gorla, M., Chang, C., Kania, A., and Bashaw, G.J. (2021). Robo recruitment of the Wave regulatory complex plays an essential and conserved role in midline repulsion. eLife *10*, e64474.
84. Chen, B., Brinkmann, K., Chen, Z., Pak, C.W., Liao, Y., Shi, S., Henry, L., Grishin, N.V., Bogdan, S., and Rosen, M.K. (2014). The WAVE regulatory complex links diverse receptors to the actin cytoskeleton. Cell *156*, 195–207.
85. Gara, R.K., Kumari, S., Ganju, A., Yallapu, M.M., Jaggi, M., and Chauhan, S.C. (2015). Slit/Robo pathway: a promising therapeutic target for cancer. Drug Discov. Today *20*, 156–164.
86. Ahammad, I. (2020). A comprehensive review of tumor proliferative and suppressive role of semaphorins and therapeutic approaches. Biophys. Rev. *12*, 1233–1247.
87. Maruyama, T., and Fujita, Y. (2017). Cell competition in mammals — novel homeostatic machinery for embryonic development and cancer prevention. Curr. Opin. Cell Biol. *48*, 106–112.
88. Tanimura, N., and Fujita, Y. (2020). Epithelial defense against cancer (EDAC). Semin. Cancer Biol. *63*, 44–48.
89. Porazinski, S., de Navascués, J., Yako, Y., Hill, W., Jones, M.R., Maddison, R., Fujita, Y., and Hogan, C. (2016). EphA2 Drives the Segregation of Ras-Transformed Epithelial Cells from Normal Neighbors. Curr. Biol. *26*, 3220–3229.
90. Hill, W., Zaragkoulias, A., Salvador-Barbero, B., Parfitt, G.J., Alatsatianos, M., Padilha, A., Porazinski, S., Woolley, T.E., Morton, J.P., Sansom, O.J., et al. (2021). EPHA2-dependent outcompetition of KRASG12D mutant cells by wild-type neighbors in the adult pancreas. Curr. Biol. *31*, 2550–2560.e5.
91. Schindelin, J., Arganda-Carreras, I., Frise, E., Kaynig, V., Longair, M., Pietzsch, T., Preibisch, S., Rueden, C., Saalfeld, S., Schmid, B., et al. (2012). Fiji: an open-source platform for biological-image analysis. Nat. Methods *9*, 676–682.
92. Herbert, S., Valon, L., Mancini, L., Dray, N., Caldarelli, P., Gros, J., Esposito, E., Shorte, S.L., Bally-Cuif, L., Aulner, N., et al. (2021). LocalZProjector and DeProj: a toolbox for local 2D projection and accurate morphometrics of large 3D microscopy images. BMC Biol. *19*, 136.
93. Sui, L., Alt, S., Weigert, M., Dye, N., Eaton, S., Jug, F., Myers, E.W., Jülicher, F., Salbreux, G., and Dahmann, C. (2018). Differential lateral and basal tension drive folding of Drosophila wing discs through two distinct mechanisms. Nat. Commun. *9*, 4620.
94. Hammer, O., Harper, D., and Ryan, P. (2001). Past: Paleontological Statistics Software Package for Education and Data Analysis. Palaeontol. Electron. *4*, 9.

STAR★METHODS

KEY RESOURCES TABLE

REAGENT or RESOURCE	SOURCE	IDENTIFIER
Antibodies		
mouse monoclonal anti-Robo1	Developmental Studies Hybridoma Bank	DSHB-13C9 RRID: AB_2181861
mouse monoclonal anti-Robo3 extracellular	Developmental Studies Hybridoma Bank	DSHB-14C9 RRID: AB_528454
mouse monoclonal anti-Robo3 cytoplasmic	Developmental Studies Hybridoma Bank	DSHB-15H2 RRID: AB_531800
mouse anti-Ds	Suzanne Eaton	N/A
mouse monoclonal anti-Nrt	Developmental Studies Hybridoma Bank	DSHB-BP106 RRID: AB_528404
mouse anti-Sema2	Developmental Studies Hybridoma Bank	DSHB-19C2 RRID: AB_528460
mouse anti-Ptc	Developmental Studies Hybridoma Bank	DSHB-Apa1 RRID: AB_528441
mouse anti-Wg	Developmental Studies Hybridoma Bank	DSHB-4D4 RRID: AB_528512
mouse monoclonal anti-β-gal	Promega	Z378B, RRID: AB_2323752
Rabbit polyclonal anti-β-gal	MP Biomedicals	55976, SKU: 085597-CF
rabbit anti-Ephrin	Andrea Brand	N/A
Rabbit polyclonal anti-Dcp1	Cell Signaling Technology	CST-9578S; RRID: AB_2721060
rabbit anti-GFP	Thermo Fisher Scientific	G10362, RRID: AB_2536526
rat anti-E-cadherin	Developmental Studies Hybridoma Bank	DSHB-DCAD2 RRID: AB_528120
rat monoclonal anti-RFP	ChromoTek	5F8 RRID: AB_2336064
Chemicals, peptides, and recombinant proteins		
DAPI	Sigma-Aldrich	D9564
Phalloidin-Alexa Fluor 405	Abcam	ab176752
Phalloidin-Alexa Fluor 488	Invitrogen	A12379
Phalloidin-Alexa Fluor 555	Sigma-Aldrich	P1951
Phalloidin-Alexa Fluor 647	Invitrogen	A22287
Experimental models: Organisms/strains		
w^{118}	David Bilder	FBal0018157
$hsflp^{122}$	Ishwar Hariharan	FBtp0001101
act>y^{+}>GAL4, UAS-GFP	David Bilder	FBti0012290
act>CD2>GAL4, UAS-RFP	David Bilder	FBal0058800
tub>CD2>GAL4, UAS-nLacZ	George Pyrowolakis	FBtp0010169
UAS-LacZ	Bloomington Drosophila Stock Center	BDSC 1776
UAS-fkh-3xHA	Martin Juenger	FBal0249318
UAS-tkv^{CA}	Bloomington Drosophila Stock Center	BDSC 36537
UAS-ey	Bloomington Drosophila Stock Center	BDSC 6294
UAS-arm^{S10}	Suzanne Eaton	FBtp0001723
UAS-ci-HA	Bloomington Drosophila Stock Center	BDSC 32570
dad^{4}-LacZ	George Pyrowolakis	FBsf0000872988
TRE-RFP	Dirk Bohmann	FBti0147636
$puc^{A251.1F3}$ >LacZ	Bloomington Drosophila Stock Center	BDSC 11173

(*Continued on next page*)

Continued

REAGENT or RESOURCE	SOURCE	IDENTIFIER
CoinFLP-LexA::GAD.GAL4	Bloomington Drosophila Stock Center	BDSC 59271
en-GAL4	Mirka Uhlirova	FBal0052377
brk-GAL4; UAS-mCD8::GFP, LexO-mCherry::CAAX/SM5-TM6b; LexO-tkv^{QD}/SM5-TM6b	George Pyrowolakis	FBal0295113
UAS-tkv-RNAi (HMS02185)	Bloomington Drosophila Stock Center	BDSC 40937
UAS-Ras^{V12}	Helena Richardson	FBtp0001705
UAS-Ras^{V12}	Bloomington Drosophila Stock Center	BDSC 4847
UAS-myc.HA	Bloomington Drosophila Stock Center	BDSC 64759
UAS-hpo	Ishwar Hariharan	FBal0191267
UAS-wts-RNAi (101055/KK)	Vienna Drosophila Resource Center	VDRC 111002
elav-GAL4, UAS-GFP	Bloomington Drosophila Stock Center	BDSC 6923
toll-2-GFP	Vienna Drosophila Resource Center	VDRC 318319
toll-8-YFP/CyO,hbLacZ	Jennifer Zallen	FBtp0148072
rst-GFP	Bloomington Drosophila Stock Center	BDSC 59410
hbs-GFP	Bloomington Drosophila Stock Center	BDSC 65321
hbs-LacZ	Ruth Johnson	FBal0131086
sns-GFP	Bloomington Drosophila Stock Center	BDSC 59801
sema1a-GFP	Bloomington Drosophila Stock Center	BDSC 50816
netA-GFP	Bloomington Drosophila Stock Center	BDSC 59409
eph-GFP	Frank Schnorrer	FlyFos015198
ten-m-GFP	Bloomington Drosophila Stock Center	BDSC 59798
ten-a-GFP	Bloomington Drosophila Stock Center	BDSC 60541
trn-LacZ	Bloomington Drosophila Stock Center	BDSC 4550
ft-EGFP	David Strutt	FBal0385338
ds-LacZ	Bloomington Drosophila Stock Center	BDSC 11394
sli-GFP	Bloomington Drosophila Stock Center	BDSC 64472
robo2-GFP	Bloomington Drosophila Stock Center	BDSC 61774
netB-GFP	Bloomington Drosophila Stock Center	BDSC 67644
unc5-GFP	Bloomington Drosophila Stock Center	BDSC 60547
UAS-robo3-HA	Bloomington Drosophila Stock Center	BDSC 66890
UAS-robo2-HA	Bloomington Drosophila Stock Center	BDSC 66886
UAS-robo2-RNAi	Bloomington Drosophila Stock Center	BDSC 34589
UAS-DEphrin	Andrea Brand	FBal0269900
UAS-eph-RNAi	Bloomington Drosophila Stock Center	BDSC 35290
UAS-ten-a	Bloomington Drosophila Stock Center	BDSC 42018
UAS-ten-m	Bloomington Drosophila Stock Center	BDSC 41570
UAS-toll-8	Yoshimasa Yagi	N/A
UAS-toll-2	Yoshimasa Yagi	N/A
UAS-netB-RNAi	Vienna Drosophila Resource Center	VDRC 100840
UAS-trn-HA	Jennifer Zallen	N/A
UAS-ft	David Strutt	FBtp0019924
UAS-ft-RNAi	Bloomington Drosophila Stock Center	BDSC 34970
UAS-ds	David Strutt	FBtp0019964
UAS-ds-RNAi (GD14350)	David Strutt	VDRC 36219
UAS-robo1-RNAi	Vienna Drosophila Resource Center	VDRC 42241
UAS-robo3-RNAi	Vienna Drosophila Resource Center	VDRC 44702
UAS-ten-m-RNAi	Bloomington Drosophila Stock Center	BDSC 29390
UAS-rst	Ruth Johnson	RJ459

(*Continued on next page*)

Continued

REAGENT or RESOURCE	SOURCE	IDENTIFIER
UAS-kirre	Karl-Friedrich Fischbach	FBtp0013068
UAS-hbs	Ruth Johnson	RJ404
UAS-eph	Mel Feany	Probably FBtp0055391, not FBtp0055389, nor FBtp0015743
UAS-plexA-RNAi (HM05221, GD/14483, GL01870, KK/101499)	Bloomington Drosophila Stock Center Vienna Drosophila Resource Center	BDSC 30483, VDRC 27240, BDSC 67845, VDRC 107004
UAS-plexB-RNAi (HM05122, GD/16420)	Bloomington Drosophila Stock Center Vienna Drosophila Resource Center	BDSC 28911, VDRC 46687
UAS-sema2a-RNAi (GL00356)	Bloomington Drosophila Stock Center	BDSC 35432
UAS-plexA	Bloomington Drosophila Stock Center	BDSC 8479
UAS-sli.D	Bloomington Drosophila Stock Center	BDSC 67689
UAS-slit-RNAi (KK/100803)	Vienna Drosophila Resource Center	VDRC 108853
UAS-cirl-RNAi (KK/108383, JF02674, HMS00136)	Vienna Drosophila Resource Center Bloomington Drosophila Stock Center	VDRC100749, BDSC 27524, BDSC 34821
UAS-tl	Bloomington Drosophila Stock Center	BDSC 58987
UAS-tl-RNAi (JF01276, JF01491)	Bloomington Drosophila Stock Center	BDSC 31477, BDSC 31044
UAS-toll-2-RNAi	Bloomington Drosophila Stock Center	BDSC 30498
UAS-toll-3	Yoshimasa Yagi	N/A
UAS-toll-3-RNAi (HM05012)	Bloomington Drosophila Stock Center	BDSC 28526
UAS-toll-4	Yoshimasa Yagi	N/A
UAS-toll-4-RNAi (HM050297)	Bloomington Drosophila Stock Center	BDSC 28543
UAS-toll-5-RNAi (HM05212)	Bloomington Drosophila Stock Center	BDSC 29533
UAS-toll-6	Yoshimasa Yagi	N/A
UAS-toll-6-RNAi (HMC0584, HMS04251)	Bloomington Drosophila Stock Center	BDSC 64968, BDSC 56048
UAS-toll-7	Yoshimasa Yagi	N/A
UAS-toll-7-RNAi (HM05230)	Bloomington Drosophila Stock Center	BDSC 30488
UAS-toll-8-RNAi	Bloomington Drosophila Stock Center	BDSC 28519
UAS-toll-9-RNAi (HM05227, HMS00171)	Bloomington Drosophila Stock Center	BDSC 30535, BDSC 34853
UAS-dachs.V5	Bloomington Drosophila Stock Center	BDSC 28814
UAS-dachs-RNAi (JF02743)	Bloomington Drosophila Stock Center	BDSC 27664
UAS-caps-RNAi (GD/2530, GD/14433, JF02854)	Vienna Drosophila Resource Center Bloomington Drosophila Stock Center	VDRC 3046, VDRC 27097, BDSC 28020
UAS-trn-RNAi (GLC01638, KK/104688, HM05011)	Vienna Drosophila Resource Center Bloomington Drosophila Stock Center	BDSC 50520, VDRC 107883, BDSC 28525
UAS-netB-RNAi (KK/103672)	Vienna Drosophila Resource Center	VDRC 100840
UAS-unc5-RNAi (HMS01099)	Bloomington Drosophila Stock Center	BDSC 33756
UAS-fra	Bloomington Drosophila Stock Center	BDSC 8814
UAS-fra-RNAi (JF01231, JF01457)	Bloomington Drosophila Stock Center	BDSC 31469, BDSC 31664
UAS-kek1-RNAi (HMC04442)	Bloomington Drosophila Stock Center	BDSC 57000
UAS-kek3-RNAi (HMS05948)	Bloomington Drosophila Stock Center	BDSC 77354
UAS-kek4-RNAi (HMC06307)	Bloomington Drosophila Stock Center	BDSC 67206
UAS-kek5-RNAi (HMS01996)	Bloomington Drosophila Stock Center	BDSC 40830
UAS-ret.L	Bloomington Drosophila Stock Center	BDSC 59002

(*Continued on next page*)

Continued		
REAGENT or RESOURCE	SOURCE	IDENTIFIER
UAS-ret-RNAi (HMC04143)	Bloomington Drosophila Stock Center	BDSC 55872
UAS-GP150 (HMS00395)	Bloomington Drosophila Stock Center	BDSC 32400
UAS-dscam4-RNAi (HMC03277)	Bloomington Drosophila Stock Center	BDSC 51508
UAS-dscam4	Bloomington Drosophila Stock Center	BDSC 17117
UAS-dscam2-RNAi (HMC03411)	Bloomington Drosophila Stock Center	BDSC 51839
UAS-pyd-RNAi	Ruth Johnson	RJ452
UAS-ics.O	Bloomington Drosophila Stock Center	BDSC 66567
UAS-sas-RNAi (KK/106177)	Vienna Drosophila Resource Center	VDRC 100901
UAS-fili-RNAi (HM05054)	Bloomington Drosophila Stock Center	BDSC 28568
UAS-bsg-RNAi (HMC03195)	Bloomington Drosophila Stock Center	BDSC 52110
UAS-con-RNAi (HM05178)	Bloomington Drosophila Stock Center	BDSC 28967
UAS-beat-VII-RNAi (HMC05049)	Bloomington Drosophila Stock Center	BDSC 60056
UAS-beat-IIIc-RNAi (JF03286)	Bloomington Drosophila Stock Center	BDSC 29607
UAS-tnc-RNAi (HMC05051)	Bloomington Drosophila Stock Center	BDSC 60058
Software and algorithms		
FIJI (ImageJ 1.48b)	Schindelin et al.[91]	https://fiji.sc/
local-z-projector Fiji plugin v1.5.4	Herbert et al.[92]	https://gitlab.pasteur.fr/iah-public/Local Zprojector
GraphPad Prism	Graph Pad	version 9.5.0
Affinity Designer	Affinity	Up to version 1.10.8
Microsoft Excel	Microsoft	Microsoft Excel 365
Procreate	Procreate	Version 5.2.9
Inkscape (0.92.4)	Inkscape	https://inkscape.org/release/inkscape-0.92.4/
Biorender	Science Suite Inc. DBA BioRender	Biorender

RESOURCE AVAILABILITY

Lead contact

Further information and requests for resources and reagents should be directed to and will be fulfilled by the lead contact, Anne-Kathrin Classen (anne.classen@biologie.uni-freiburg.de).

Materials availability

This study did not generate new unique reagents.

Data and code availability

- Quantitative data sets are provided as supplemental source files with this publication. Raw imaging data reported in this paper will be shared by the lead contact upon request.
- This paper does not report original code.
- Any additional information required to reanalyze the data reported in this paper is available from the lead contact upon request.

EXPERIMENTAL MODEL

All experiments were performed on *Drosophila melanogaster*. Fly strains (see key resources table) were maintained on standard fly food (10L water, 74,5g agar, 243g dry yeast, 580g corn flour, 552ml molasses, 20.7g Nipagin, 35ml propionic acid) at 18°C – 22°C. Larvae from experimental crosses were allowed to feed on Bloomington formulation (175.7g Nutry-Fly,1100ml water 20g dry yeast, 1.45g Nipagin in 15ml Ethanol, 4.8ml Propionic acid) and raised at 25°C. Our experimental design did not consider differences between sexes unless for genetic crossing schemes.

METHOD DETAILS

Drosophila genetics

Mosaic gene expression was induced by Flip-out (act or tub>GAL4/UAS, CoinFLP-LexA/LexO) or mitotic FLP/FRT.[39,71] Parental adult flies were allowed to lay eggs for 72 h at 25°C before flippase expression was induced by heat shock (HS) at 37°C for

5-15 min. Detailed genotypes and experimental conditions are listed in Table S1. For the JNK interface signaling screen (Figure S1F), larvae were dissected 48 h after a 10 min HS (AHS). Due to genetic limitations, the CoinFLP experiments (Figures S7H–S7J) contained two GAL4-drivers, the Actin5C-FRT/STOP-GAL4 and the *en*-GAL4, resulting in mosaic GAL4 expression in the total disc and GAL4 expression in the posterior compartment. For experiments examining expression patterns (Figures 2 and S2), larvae were dissected 80 h or 102 h after egg lay (AEL).

Immunohistochemistry

Larvae were dissected and the inverted cuticula with attached wing discs were fixed in 4% paraformaldehyde in PBS for 15 min at 22°C. Samples were washed in 0.1% Triton X-100 in PBS (PBT) and incubated with primary and secondary antibodies in 400µl PBT on a nutator overnight at 4°C and 1-3 h at 22°C, respectively. Following a final wash in PBS, wing discs were mounted with Molecular Probes Antifade Reagents (#S2828). Following antibodies were used: Mouse anti-Robo1 (1:20, DSHB-13C9), mouse anti-Robo3 (1:20, DSHB-14C9&15H2), mouse anti-Ds (1:1000, Suzanne Eaton), mouse anti-Nrt (1:20, DSHB-BP106), mouse anti-Sema2 (1:20, DSHB-19C2), mouse anti-Ptc (1:20, DSHB-apa1), mouse anti-Wg (1:100, DSHB-4D4), rabbit anti-Ephrin (1:1000, Andrea Brand), rabbit anti-Dcp1 (1:400, Cell Signaling-9578S), rat anti-E-cadherin (1:50, DSHB-DCAD2), mouse anti-β-gal (1:1000, Promega Z378B), mouse anti-β-gal (1:1000, MP Biochemicals-55976), rabbit anti-HA (1:200, Invitrogen 715500), rabbit anti-GFP (1:400, Thermo Fisher-G10362), rat anti-RFP (1:20, Heinrich Leonhardt, 5F8) and rat anti-RFP (1:2000, ChromoTek-5F8). Fluorescent dyes DAPI (0.25 ng/µl, Sigma), Phalloidin-Alexa Fluor 405 (1:2000, Abcam-ab176752), Phalloidin-Alexa Fluor 488 (1:500, Invitrogen A12379), Phalloidin-Alexa Fluor 555 (1:500, sigma-P1951) and Phalloidin-Alexa Fluor 647 (1:500, Invitrogen A22287) were added together with secondary antibodies.

Image acquisition and image display

Samples were imaged using Leica TCS SP8 confocal microscopes. Figure panels were assembled in Affinity Designer. In most figure panels, individual channels represent the same z-position from a confocal image stack. However, some panels may assemble channels from different z-positions in the wing disc (as listed in Table S2). Such a portrayal was chosen to better visualize the spatially distinct phenotypes at different positions within the cell, specifically of (1) junctional actin (apical), (2) cytoplasmic/nuclear RFP (lateral) and (3) Dcp1 (basal) in one image panel. This was meant to reduce the (peripheral) data load in the manuscript that would be otherwise required to visualize all channels at all positions.

If mentioned in the figure legends, the local-z-projector Fiji plugin (https://gitlab.pasteur.fr/iah-public/Local Zprojector, v1.5.4)[92] was used to project the curved apical surface of the wing disc epithelium into the same plane. The local-z-projector generates a surface height-map based on a reference channel (i.e., Ecad or Phalloidin staining) and other channels of interest were displayed in relation to this surface height-map.

Illustration of expression patterns

Procreate (Version 5.2.9) was used for illustration of cell surface receptor expression patterns (Figure 2). Characteristic points of reference, such as hinge folds, A/P and D/V boundary, were used to transfer the expression domains manually into a wing disc template. The grading of fluorescence intensity is based on overall impression of intensity across the wing disc and is presented as a subjective approximation. Bitmap tracing was done in Inkscape (0.92.4) to convert the areas of expression into vector graphics.

IMAGE QUANTIFICATION AND STATISTICAL ANALYSIS

To provide a measure for reproducibility and robustness, number of samples (wing discs) and experimental replicates are mentioned in the figure legends. An experimental replicate refers to an independent event for dissection and sample processing. From each larva, only one wing disc per larva was dissected and considered to be an independent sample for statistical analysis. Please note that several discs were visually analyzed for each experimental replicate. For all quantifications, control and experimental samples were processed together and imaged in parallel, using the same confocal settings. For comparison of TRE-RFP and Dcp1 fluorescence intensities in different bands around the clone, a repeated measured one-way ANOVA with Tukey's multiple comparisons test was used. Kruskal-Wallis test with Dunnett's multiple comparison test was used for comparison of changes in Robo2-GFP intensities in aberrant clones. For other comparisons, a two tailed, unpaired t-test was performed. Images were processed in FIJI.[91] GraphPad Prism (version 9.5.0) was used for statistical analysis and generation of graphs. Source data for our statistical analysis is provided in Data S1, S2, S3, and S4.

Region of interest (ROI) segmentation and quantification workflow

(ROI1) of total disc area: RFP or Phalloidin signal was thresholded and the ROI created by Convert to Mask, Fill Holes, and selection by the wand tool. (ROI2) of clone area: clonal GFP signal was thresholded and ROIs were created by analyze particles=10µm-infinity. For Dcp1 quantification, the lower cutoff was 2µm. (ROI3) WT cells at interface: the Make Band, 4µm command created a band around the ROI2. (ROI4) clonal cells not at the interface: the Enlarge, -4µm command applied on ROI2 created a ROI of the inner clone area. (ROI5) Clonal cells at the interface: XOR of ROI2 and ROI4. (ROI6) WT area around the ROI3: First, Make Band, 16µm created a band around ROI2. XOR of this band and ROI3 resulted in ROI6.

Subsequent general procedures: by using the Combine command, several ROIs of a category, such as individual clones in ROI2, were combined to one ROI and used for further analysis. Signal outside the wing disc was excluded by AND of ROI1 and other ROIs. ROIs of WT cells, such as ROI3 and ROI6, might cover clonal area due to insufficient spacing of clones. This was prevented, in example for ROI3, by first selecting OR of ROI3 and ROI2, followed by XOR of that selection and ROI2. After the disc segmentation into ROIs, the Measure command was applied.

Workflow for quantification of TRE-RFP intensity in UAS-eph-RNAi and UAS-GFP clones

7min HS at 37°C, 72 h AEL, reared at 25°C, dissected 72 h AHS. TRE-RFP signal was elevated by anti-RFP antibody staining. One lateral section was imaged and quantified. Area and mean intensity of TRE-RFP was measured in each ROI. For circularity, the shape of individual clones in ROI2 was measured.

Workflow for quantification of TRE-RFP intensity in UAS-robo2-HA and UAS-GFP clones

8min HS at 37°C, 72 h AEL, reared at 25°C, dissected 48 h AHS. TRE-RFP signal with and without rat anti-RFP antibody was compared (Figure S3). One lateral section of native TRE-RFP was imaged and quantified. Area and mean intensity of TRE-RFP was measured in each ROI. For circularity, the shape of individual clones in ROI2 was measured.

Workflow for quantification of Dcp1 intensity in UAS-robo2-HA and UAS-GFP clones

9min HS at 37°C, 72 h AEL, reared at 25°C, dissected 30 h AHS. In total, 4 confocal z-sections were quantified. As apoptotic cells are localized basally, imaging of the stack was started at the most basal position, moving towards the apical surface in 2μm steps, resulting in the quantification of basal and lateral sections. The above-described ROI segmentation and measurement of Dcp1 intensity was applied individually for each z-section in all ROIs. Eventually, the intensities of all four z-sections were averaged before doing the statistics.

Workflow for quantification of TRE-RFP and Dcp1 intensity in UAS-robo3-HA and UAS-GFP clones

19min HS at 37°C,72h AEL, reared at 25°C, dissected 48 h AHS. The workflow for the quantification of Dcp1 was as described in DCP1 quantification for *UAS-robo2-HA*. TRE-RFP intensities were quantified for the second most apical slice of the z-stack.

Workflow for quantification of TRE-RFP intensities in the wing disc notum with UAS-robo2-RNAi alone or with expression with UAS-robo3-HA

13min HS at 37°C, 80h AEL, reared at 25°C, dissected 40h AHS. Of a z-stack, the z-position with best aerial coverage of the epithelial cells of the wing disc notum was selected. The anterior-notum area was manually converted into a ROI and TRE-RFP intensities were measured as mentioned before, but only within this ROI.

Workflow for quantification of Robo2-GFP regulation in UAS-GFP, UAS-ey, UAS-tkv-RNAi, UAS-fkh clones

Crosses: 10min HS at 37°C, 72 h AEL, reared at 25°C, dissected 44 h AHS. Confocal z-stack had a step size of 4μm. Of those, 4 contiguous lateral z-sections beneath the peripodium were chosen for quantification. First, the wing disc was manually separated into approximate pouch, hinge and notum areas by using the polygon selections in Fiji. For the pouch, a shape was drawn along the apical hinge-pouch fold. For the notum, the apical hinge-notum fold and wing disc outline was used.[93] The area between those two areas and the wing disc outline was used as hinge area. Then, the above-described ROI segmentation with measurement of Robo2-GFP intensity in ROI3 and ROI5 was applied individually for each z-section. The results were then processed as follows. Individual clones were tracked through the z-stack by their centroids and the Similarity And Distance Indices function in Past4,[94] resulting in up to 4 data points per clone. To avoid non genotype specific changes in Robo2-GFP intensity due to cyst formation and consequent changes of the apical plane in clones, the data points were filtered based on changes in actin levels. Data points from z-sections in which the clone had actin changes of >20% between ROI3 and ROI5, while Robo2-GFP intensity increased, were excluded. Vice versa, clones with actin changes of <-20% between ROI3 and ROI5, while Robo2-GFP intensity decreased, were excluded as well. Furthermore, small clones beneath 30μm^2 were excluded, as well as clones which were only detected in one of the 4 z-sections. Eventually, the data point of a clone, which was used for further statistics, derived from the most apical z-section that fulfilled all those criteria.

Current Biology, Volume *34*

Supplemental Information

A mismatch in the expression of cell surface molecules induces tissue-intrinsic defense against aberrant cells

Friedericke Fischer, Laurin Ernst, Anna Frey, Katrin Holstein, Deepti Prasad, Vanessa Weichselberger, Ramya Balaji, and Anne-Kathrin Classen

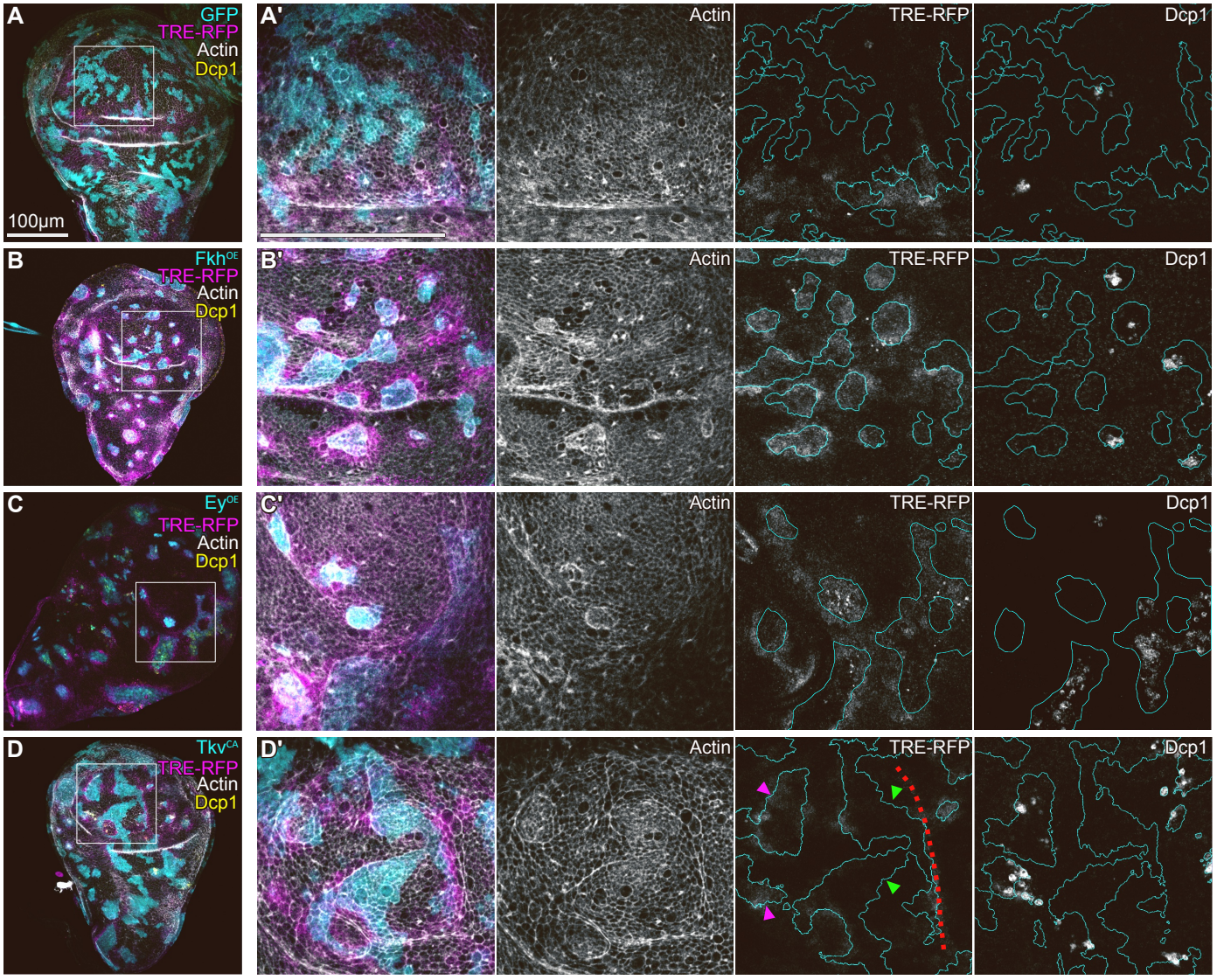

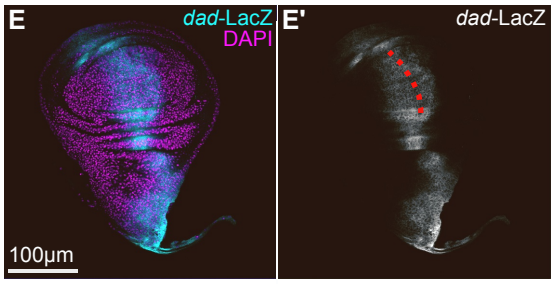

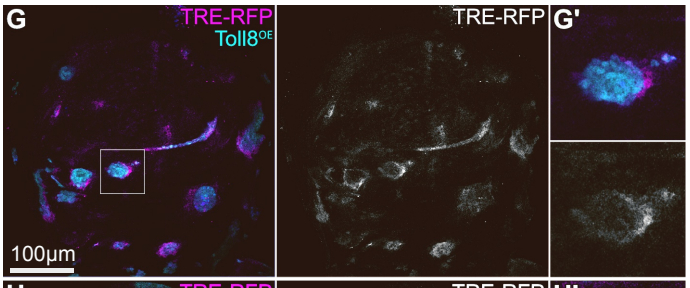

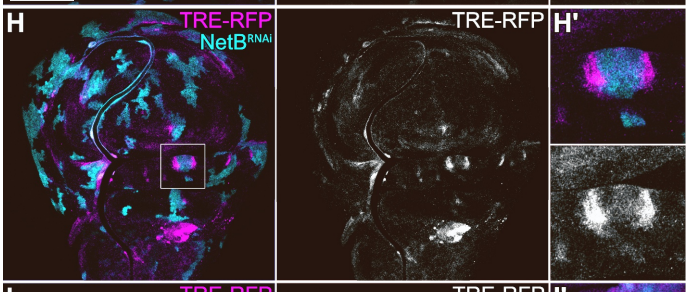

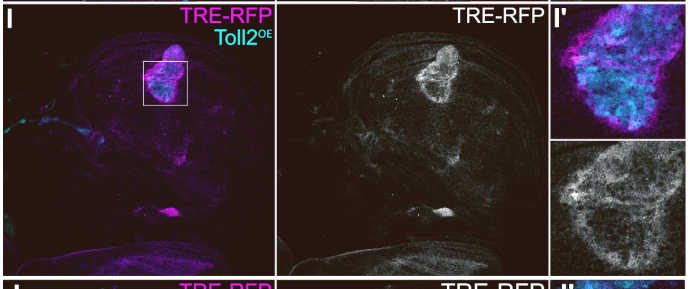

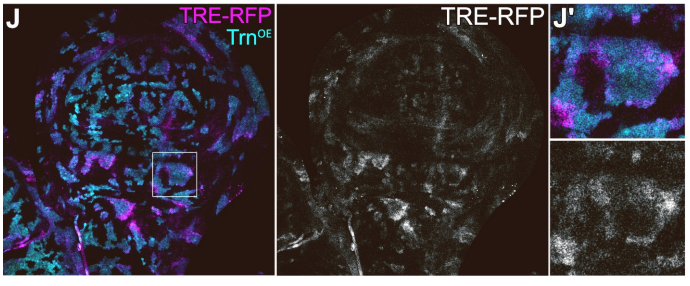

F

	OE	RNAi
Robo1	NA	
Robo2		
Robo3		
Slit		
Eph		
Ephrin		NA
Ten-m		
Ten-a		NA
Tl		
Toll2		
Toll3		
Toll4		
Toll5	NA	
Toll6		
Toll7		
Toll8		
Toll9	NA	
Ds		
Ft		
Dachs		
Caps	NA	
Trn		
NetB	NA	
Unc5	NA	
Fra		

	OE	RNAi
Rst		NA
Hbs		NA
Kirre		NA
PlexA		
PlexB	NA	
Sema2a	NA	
Ret		
Kek	NA	
Fwe$_{LoseA}$		NA
Fwe$_{LoseB}$		NA
GP150	NA	
Dscam4		
Dscam2	NA	
Pyd	NA	
Ics		NA
Sas	NA	
Fili	NA	
Bsg	NA	
Con	NA	
Beat-VII	NA	
Beat-IIIC	NA	
Tnc	NA	
Cirl	NA	

no TRE-RFP response
interface TRE-RFP response
other TRE-RFP responses
NA not assessed

Figure S1. Hallmarks of interface surveillance in response to clones with aberrant cell fate. Related to Figure 1.

A-D Mosaic wing disc with wild type clones expressing *UAS-GFP* (GFP) (A), or with clonal alterations in fate specifying pathways by ectopic expression of Fkh (Fkh^{OE}) (B), Ey (Ey^{OE}) (C), or expression of a constitutively active Tkv (Tkv^{CA}) (D) using the 'GAL4/UAS flp-out' system. TRE-RFP expression is reporting JNK pathway activity (grey or magenta in A-D). Antibody staining against the cleaved effector caspase (cDcp1) visualizes apoptosis (grey or yellow in A-D). Cortical F-actin was visualized by Phalloidin (grey). White frame marks regions shown in (A'-D').
Green and magenta arrows indicate clone interfaces in and outside Dpp signaling domain (E), respectively.

E Wing disc expressing the transcriptional reporter *dad*-LacZ, a target gene of the morphogen Dpp. Red dotted line represents the A/P compartment boundary. Previous work showed that Tkv^{CA} clones do not induce JNK boundary response in the Dpp-signaling domain (Prasad et al, 2023, Elife).

F Summary of the candidate screen for JNK interface signaling induced by either ectopic expression (^{OE}) of *UAS* constructs or downregulation of expression by *UAS-RNAi* (^{RNAi}) constructs for individual cell surface molecules (see **key resource table** for detailed constructs). The TRE-RFP reporter was used to access induction of JNK interface signaling at clone boundaries. Phenotypes of TRE-RFP responses were categorized in three groups: JNK interface signaling at clone boundaries (See **Figure 1** for representative images), other TRE-RFP responses (for example, intra-clonal activation) and no TRE-RFP responses (phenotypes not shown).

G-J Mosaic wing discs with aberrant expression of cell surface molecules. Clones express GFP (cyan) and were exposed to either ectopic expression (^{OE}) of *UAS* constructs or downregulation of expression by *UAS-RNAi* (^{RNAi}) constructs for individual cell surface molecules, as indicated in each panel. White frame marks regions shown in (G'-J').

Related images are shown at same scale with a scale bar of 100µm.

A

80 h | 102 h | 80 h | 102 h

Eph^{GFP} αPtc & αWg | Eph^{GFP} | Eph^{GFP} αPtc & αWg | Eph^{GFP} | Toll2^{GFP} αPtc & αWg | Toll2^{GFP} | Toll2^{GFP} αPtc & αWg | Toll2^{GFP}

100μm | 100μm | 100μm | 100μm

Ten-m^{GFP} αPtc & αWg | Ten-m^{GFP} | Ten-m^{GFP} αPtc & αWg | Ten-m^{GFP} | Toll8^{YFP} αPtc & αWg | Toll8^{YFP} | Toll8^{YFP} αPtc & αWg | Toll8^{YFP}

Ten-a^{GFP} αPtc & αWg | Ten-a^{GFP} | Ten-a^{GFP} αPtc & αWg | Ten-a^{GFP} | Rst^{GFP} αPtc & αWg | Rst^{GFP} | Rst^{GFP} αPtc & αWg | Rst^{GFP}

trn-LacZ Dapi | *trn*-LacZ | *trn*-lacZ Dapi | *trn*-LacZ | Hbs^{GFP} αPtc & αWg | Hbs^{GFP} | Hbs^{GFP} αPtc & αWg | Hbs^{GFP}

Ft^{GFP} αPtc & αWg | Ft^{GFP} | Ft^{GFP} αPtc & αWg | Ft^{GFP} | *hbs*-LacZ αPtc & αWg | *hbs*-LacZ | *hbs*-LacZ αPtc & αWg | *hbs*-LacZ

αDs Actin | αDs | αDs Actin | αDs | Sns^{GFP} αPtc & αWg | Sns^{GFP} | Sns^{GFP} αPtc & αWg | Sns^{GFP}

ds-LacZ αPtc & αWg | *ds*-LacZ | *ds*-LacZ αPtc & αWg | *ds*-LacZ | Sema1^{GFP} αPtc & αWg | Sema1^{GFP} | Sema1^{GFP} αPtc & αWg | Sema1^{GFP}

Slit^{GFP} Actin | Slit^{GFP} | Slit^{GFP} Actin | Slit^{GFP} | αSema2 Actin | αSema2 | αSema2 Actin | αSema2

Robo2^{GFP} αPtc & αWg | Robo2^{GFP} | Robo2^{GFP} αPtc & αWg | Robo2^{GFP} | NetA^{GFP} αPtc & αWg | NetA^{GFP} | NetA^{GFP} αPtc & αWg | NetA^{GFP}

αRobo1 Actin | αRobo1 | αNrt Actin | αNrt | αNrt Actin | αNrt

αRobo3 Ecad | αRobo3

100μm

B

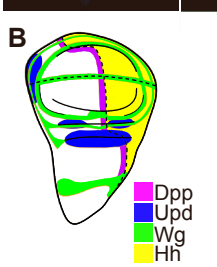

Figure S2. Expression patterns of cell surface molecules. Related to Figure 2.

A Wing discs expressing GFP-tagged fusion proteins or LacZ transcriptional reporters or stained with antibodies to detect protein expression patterns at 80 h and 102 h AEL. Ptc and Wg demarcate A/P and D/V compartment boundaries. F-actin visualizes wing disc area. All 80 h AEL discs are displayed at the same scale. All 102 h AEL discs are displayed at the same scale.

B Illustration of expression domains of fate-specifying signaling ligands, i.e., the morphogens Dpp (magenta), Wg (green), Hh (yellow) and Upd (blue). Please note that fate specifying signaling ligands also act non-autonomously by establishing morphogen gradients, and thereby specify fate patterns in the wing discs.

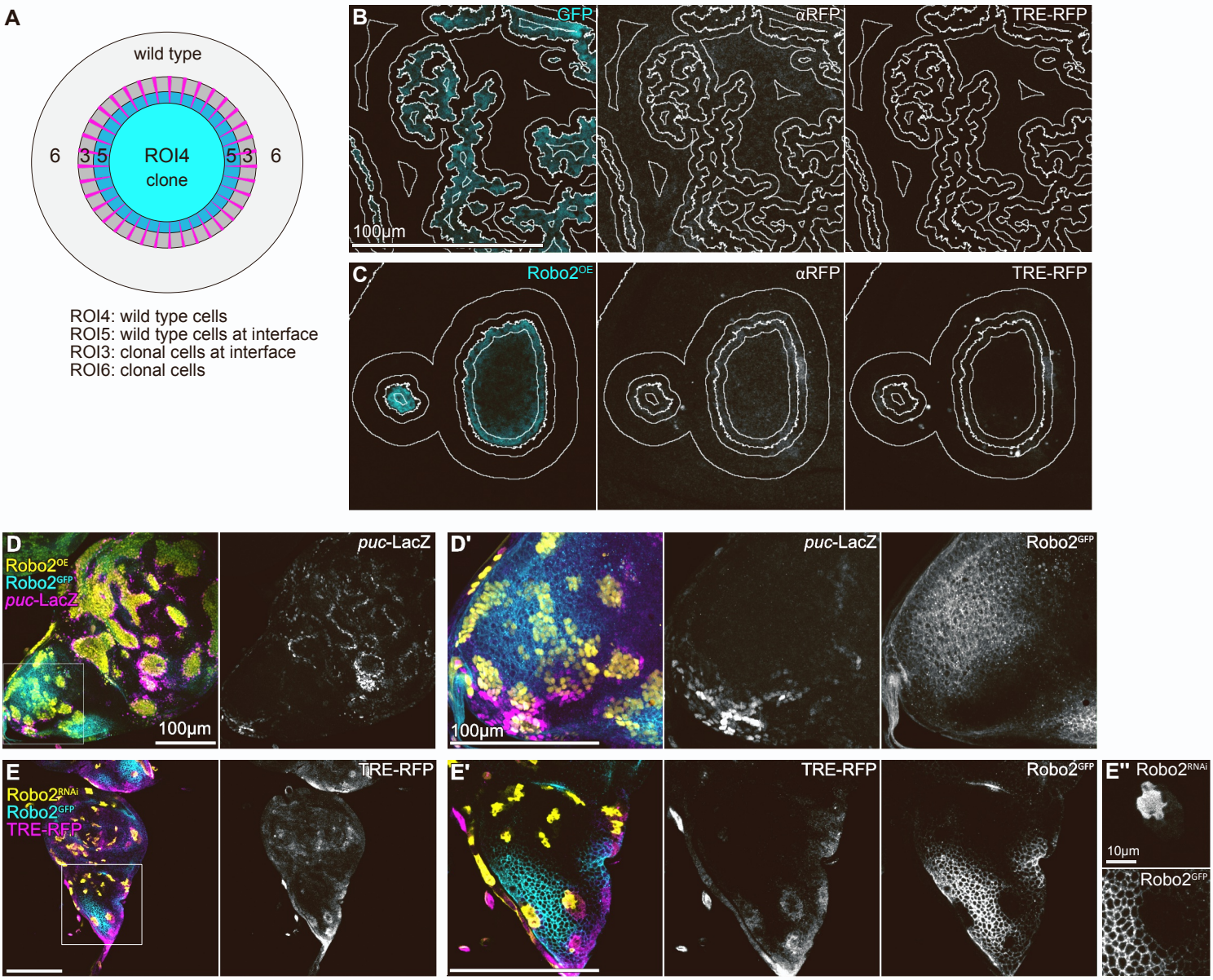
A
wild type
6
3
5
ROI4
clone
5
3
6
ROI4: wild type cells
ROI5: wild type cells at interface
ROI3: clonal cells at interface
ROI6: clonal cells
B
GFP
αRFP
TRE-RFP
100μm
C
Robo2OE
αRFP
TRE-RFP
D
Robo2OE
Robo2GFP
puc-LacZ
100μm
puc-LacZ
D'
puc-LacZ
Robo2GFP
100μm
E
Robo2RNAi
Robo2GFP
TRE-RFP
TRE-RFP
E'
TRE-RFP
Robo2GFP
E''
Robo2RNAi
10μm
Robo2GFP

Figure S3. Pattern-specific interface surveillance responses. Related to Figure 3.

A Illustration of segmented regions of interests (ROIs) as also described in (**Figure 3F**): clonal cells, that are not in touch with the interface (ROI4), a 4µm band of clonal cells (ROI5) and wild type cells (ROI3) at the interface and a 12µm band of wild type cells (ROI6) surrounding the previous ROIs (see Methods). Segmentation of the clonal interface provides the starting point for ROI annotation and subsequent measurements.

B,C Mosaic wing discs with *UAS-GFP* expressing (D) or *UAS-robo2* ($Robo2^{OE}$) (E) expressing clones. TRE-RFP expression is reporting JNK pathway activity. In addition to native TRE-RFP signal, anti-RFP antibody (αRFP) was used to enhance the TRE-RFP signal. White lines represent ROI segmentation.

D,E Wing discs expressing the *robo2-GFP* fusion protein ($Robo2^{GFP}$) under native regulatory control (grey or cyan). Mosaic clones (yellow) were induced that either express *UAS-robo2* ($Robo2^{OE}$) (D) or downregulate Robo2 using expression of *UAS-robo2-RNAi* ($Robo2^{RNAi}$) (E). Please note the reduced Robo2 expression level within clones in (E''). *puc*-LacZ (D) or TRE-RFP (E) expression (grey or magenta) is reporting JNK pathway activity (grey or magenta). Image sets are shown at the same scale. White frame marks region shown in (D', E').

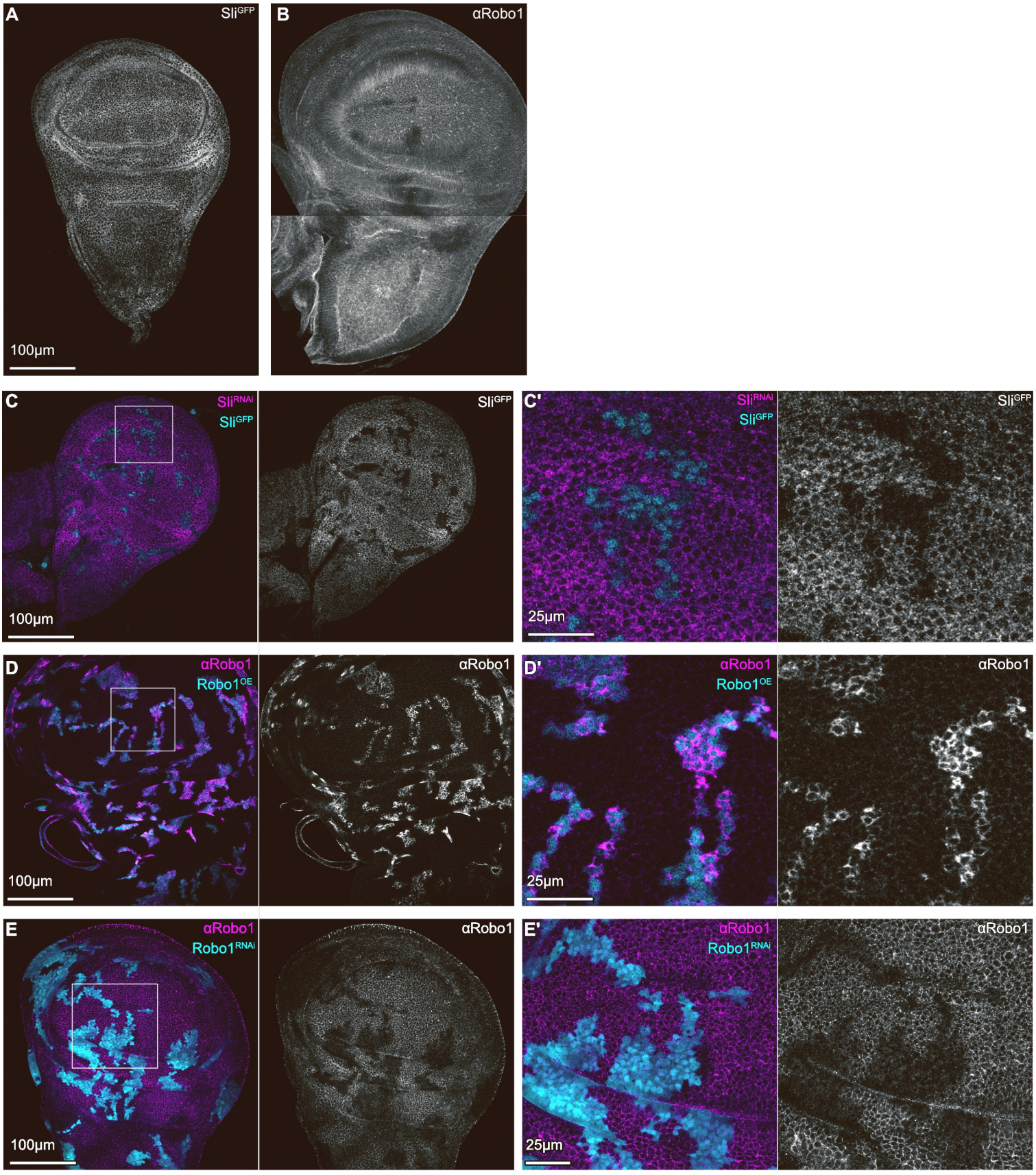
A
Sli^GFP
100µm
B
αRobo1
C
Sli^RNAi
Sli^GFP
100µm
Sli^GFP
C'
Sli^RNAi
Sli^GFP
25µm
Sli^GFP
D
αRobo1
Robo1^OE
100µm
αRobo1
D'
αRobo1
Robo1^OE
25µm
αRobo1
E
αRobo1
Robo1^RNAi
100µm
αRobo1
E'
αRobo1
Robo1^RNAi
25µm
αRobo1

Figure S4. Validation of Slit and Robo1 genetic constructs. Related to Figure 4.

A Wing disc expressing *Sli-GFP* (Sli^{GFP}) fusion protein construct under native regulatory control.

B Wing disc stained with an antibody to detect protein expression patterns of Robo1 (αRobo1).

C Mosaic wing disc expressing *Sli-GFP* (Sli^{GFP}) (magenta or grey) fusion protein construct under native regulatory control with clones (cyan) expressing *UAS-sli-RNAi* (Sli^{RNAi}). White frame marks region shown to the right in (C').

D, E Mosaic wing discs with clones (cyan) expressing *UAS-Robo1* ($Robo1^{OE}$) (D) or *UAS-Robo1-RNAi* ($Robo1^{RNAi}$) (E) stained with an antibody to detect protein expression of Robo1 (αRobo1) (magenta or grey). White frame marks region shown in (D' and E').

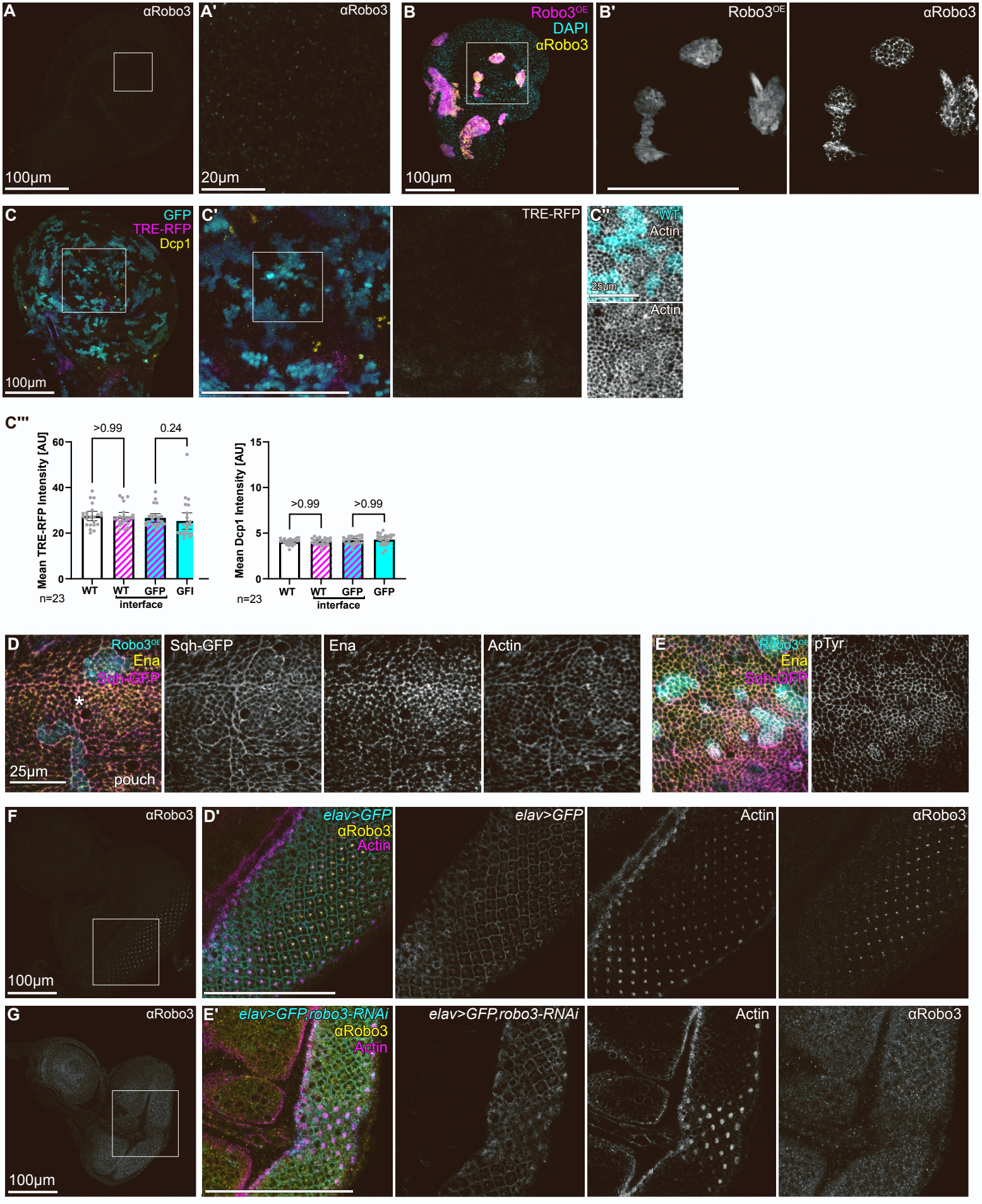
A
αRobo3
100μm
A'
αRobo3
20μm
B
Robo3OE
DAPI
αRobo3
100μm
B'
Robo3OE
αRobo3
C
GFP
TRE-RFP
Dcp1
100μm
C'
TRE-RFP
C''
WT
Actin
25μm
Actin
C'''
Mean TRE-RFP Intensity [AU]
>0.99
0.24
WT
WT
GFP
GFP
interface
n=23
Mean Dcp1 Intensity [AU]
>0.99
>0.99
WT
WT
GFP
GFP
interface
n=23
D
Robo3OE
Ena
Sqh-GFP
25μm
pouch
Sqh-GFP
Ena
Actin
E
Robo3OE
Ena
Sqh-GFP
pTyr
F
αRobo3
100μm
D'
elav>GFP
αRobo3
Actin
elav>GFP
Actin
αRobo3
G
αRobo3
100μm
E'
elav>GFP,robo3-RNAi
αRobo3
Actin
elav>GFP,robo3-RNAi
Actin
αRobo3

Figure S5. Validation of genetic tools for Robo3. Related to Figure 5.

A Wing imaginal disc stained by an anti-Robo3 antibody to visualize low level expression and punctate localization of Robo3. White frame marks region shown in (A').

B Mosaic wing disc with clones (magenta or grey) expressing *UAS-robo3* (Robo3^{OE}) and stained by an anti-Robo3 (αRobo3) (yellow or gray) antibody and DAPI (cyan or grey). White frame marks region shown in (B').

C A mosaic wing disc with wild type clones expressing *UAS-GFP* (GFP, cyan). TRE-RFP expression is reporting JNK pathway activity (grey or magenta). Antibody staining against the cleaved effector caspase (cDcp1) visualizes apoptosis (yellow). Phalloidin visualizes cortical F-actin (grey). White frame marks region shown in (C'). Please note that JNK activity is physiologically elevated at the A/P compartment boundary in wing discs at this developmental stage.

C''' Graph depicting mean fluorescence intensity of TRE-RFP reporter and mean cDcp1 intensity in the zones of measurement around clones, as depicted in (**Figure 3F**). Graphs display results for mosaic discs containing *UAS-GFP* (GFP) expressing clones. See **Figure 5** for comparison with other genotypes.
Sample number (n) for individual wing discs and p-values of a repeated measured one-way ANOVA with Tukey's multiple comparisons test are displayed in graphs. Error bars represent mean and 95% confidence interval.

D,E Mosaic wing disc with clones expressing *UAS-RFP* and *UAS-robo3* (Robo3^{OE}) (cyan) in the pouch of a wing disc. In (D): A GFP-tagged Non-muscle Myosin II regulatory light chain (Sqh-GFP) tracks the actin motor Myosin II. Antibody staining against Enabled (Ena) visualizes localization of the Drosophila Ena/Vasp actin polymerase. Phalloidin visualizes cortical F-actin. In (E): Antibody staining against phosphorylated Tyrosine (pTyr) is thought to visualize enhanced signaling activity at cellular junctions. The star marks the endogenous anterior-posterior compartment boundary. Image sets are shown at the same scale. Projections of the apical junctional network were generated using the LocalZ-projector.

F,G Eye imaginal discs with *elav*-GAL4 driven expression of *UAS-GFP* (F) or *UAS-GFP* and *UAS-robo3-RNAi* (G). Robo3 was visualized using an anti-Robo3 (αRobo3) antibody. Phalloidin visualizes cortical F-actin. Please note that Robo3 localizes to the center of assembling ommatidia clusters, which is reduced by expression of *robo3-RNAi*. White frame marks region shown in (F', G'). Image sets are shown at the same scale in (F,G) and (F',G') with a scale bar of 100µm.

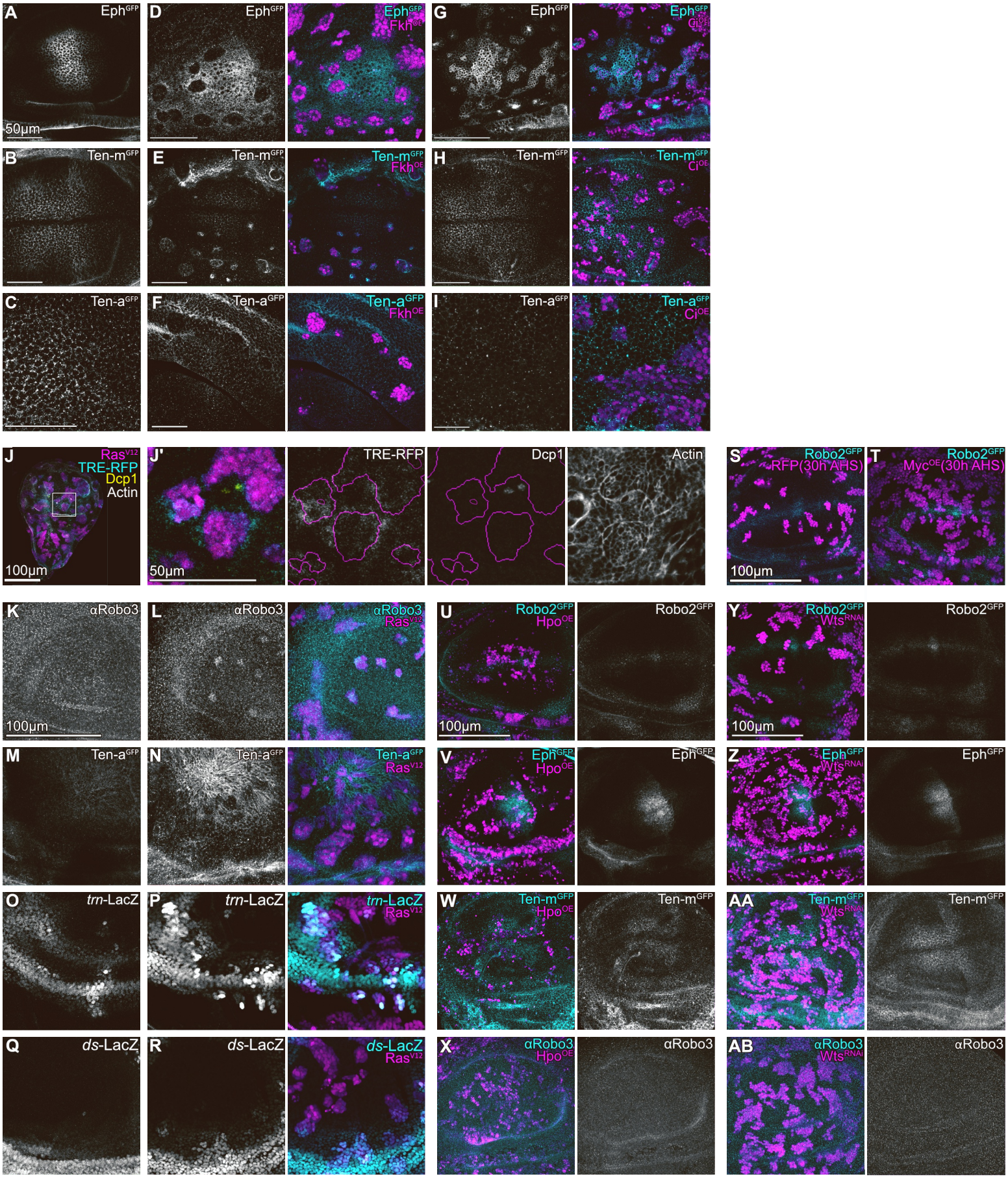
A
Eph^GFP
50μm
D
Eph^GFP
Eph^GFP Fkh^OE
G
Eph^GFP
Eph^GFP Ci^OE
B
Ten-m^GFP
E
Ten-m^GFP
Ten-m^GFP Fkh^OE
H
Ten-m^GFP
Ten-m^GFP Ci^OE
C
Ten-a^GFP
F
Ten-a^GFP
Ten-a^GFP Fkh^OE
I
Ten-a^GFP
Ten-a^GFP Ci^OE
J
Ras^V12
TRE-RFP
Dcp1
Actin
100μm
J'
50μm
TRE-RFP
Dcp1
Actin
S
Robo2^GFP
RFP(30h AHS)
100μm
T
Robo2^GFP
Myc^OE(30h AHS)
K
αRobo3
100μm
L
αRobo3
αRobo3 Ras^V12
U
Robo2^GFP Hpo^OE
Robo2^GFP
100μm
Y
Robo2^GFP Wts^RNAi
Robo2^GFP
100μm
M
Ten-a^GFP
N
Ten-a^GFP
Ten-a^GFP Ras^V12
V
Eph^GFP Hpo^OE
Eph^GFP
Z
Eph^GFP Wts^RNAi
Eph^GFP
O
trn-LacZ
P
trn-LacZ
trn-LacZ Ras^V12
W
Ten-m^GFP Hpo^OE
Ten-m^GFP
AA
Ten-m^GFP Wts^RNAi
Ten-m^GFP
Q
ds-LacZ
R
ds-LacZ
ds-LacZ Ras^V12
X
αRobo3 Hpo^OE
αRobo3
AB
αRobo3 Wts^RNAi
αRobo3

Figure S6. Expression of cell surface molecules in wing discs is regulated by fate-patterning pathways but not by cell competition. Related to Figure 6.

A-C Wing discs presenting the specific expression patterns of *eph-GFP* (Eph^{GFP}) (A), *ten-m-GFP* ($Ten\text{-}m^{GFP}$) (B) or *ten-a-GFP* ($Ten\text{-}a^{GFP}$) (C) serving as a reference pattern for the experimentally induced changes in (D-I).

D-I Wing discs expressing *eph-GFP* (Eph^{GFP}) (D), *ten-m-GFP* ($Ten\text{-}m^{GFP}$) (E), or *ten-a-GFP* ($Ten\text{-}a^{GFP}$) (F) (grey or cyan). Mosaic clones (magenta) deregulate fate-specifying pathway by expression of Fkh (Fkh^{OE}) (D-F) or by expression of Ci (Ci^{OE}) (G-I). Image sets are shown at the same scale with a scale bar of 50µm.

J Mosaic wing disc with clones deregulating EGF/ERK-signaling by expression of an oncogenic Ras, using the *UAS-RasV12* (Ras^{V12}) (magenta) construct. TRE-RFP expression is reporting JNK pathway activity (grey or cyan). Antibody staining against the cleaved effector caspase (cDcp1) visualizes apoptosis (grey or yellow). Phalloidin (grey) visualizes cortical F-actin. White frame marks region shown in (J'). Outline of clonal marker in magenta.

K,M,O,Q Wing discs presenting the specific expression patterns of Robo3 (αRobo3) (K), *ten-a-GFP* ($Ten\text{-}a^{GFP}$) (M), *trn-LacZ* (O) or *ds-LacZ* (Q), serving as a reference pattern for the experimentally induced changes in (L,N,P,R).

L,N,P,R Wing discs presenting the specific expression patterns of Robo3 (αRobo3) (L), *ten-a-GFP* ($Ten\text{-}a^{GFP}$) (N), *trn-LacZ* (P) *or ds-LacZ* (R) (grey or cyan) and carrying mosaic clones (magenta) expressing oncogenic *UAS-RasV12* (Ras^{V12}).

S,T Wing discs expressing *robo2-GFP* ($Robo2^{GFP}$), that carry mosaic clones expressing *UAS-RFP* (RFP) (S) or *UAS-Myc* (Myc^{OE}) (T). Both wing discs were dissected 30h after heat shock (AHS).

U-X Wing discs expressing *robo2-GFP* ($Robo2^{GFP}$) (U), *eph-GFP* (Eph^{GFP}) (V), *ten-m-GFP* ($Ten\text{-}m^{GFP}$) (W) or stained for Robo3 (X), and carrying mosaic clones expressing Hippo (Hpo^{OE}). Hippo expression reduces Yorkie function and thus, gives rise to loser cells.

Y-AB Wing discs expressing *robo2-GFP* ($Robo2^{GFP}$) (Y), *eph-GFP* (Eph^{GFP}) (Z), *ten-m-GFP* ($Ten\text{-}m^{GFP}$) (AA) or stained for Robo3 (AB), and carrying mosaic clones expressing *UAS-wts-RNAi* (wts^{RNAi}). Knocking down *warts* function activates Yorkie and thus gives rise to super competitor/winner cells.

Images (K-R) and (U-AB) are shown at the same scale.

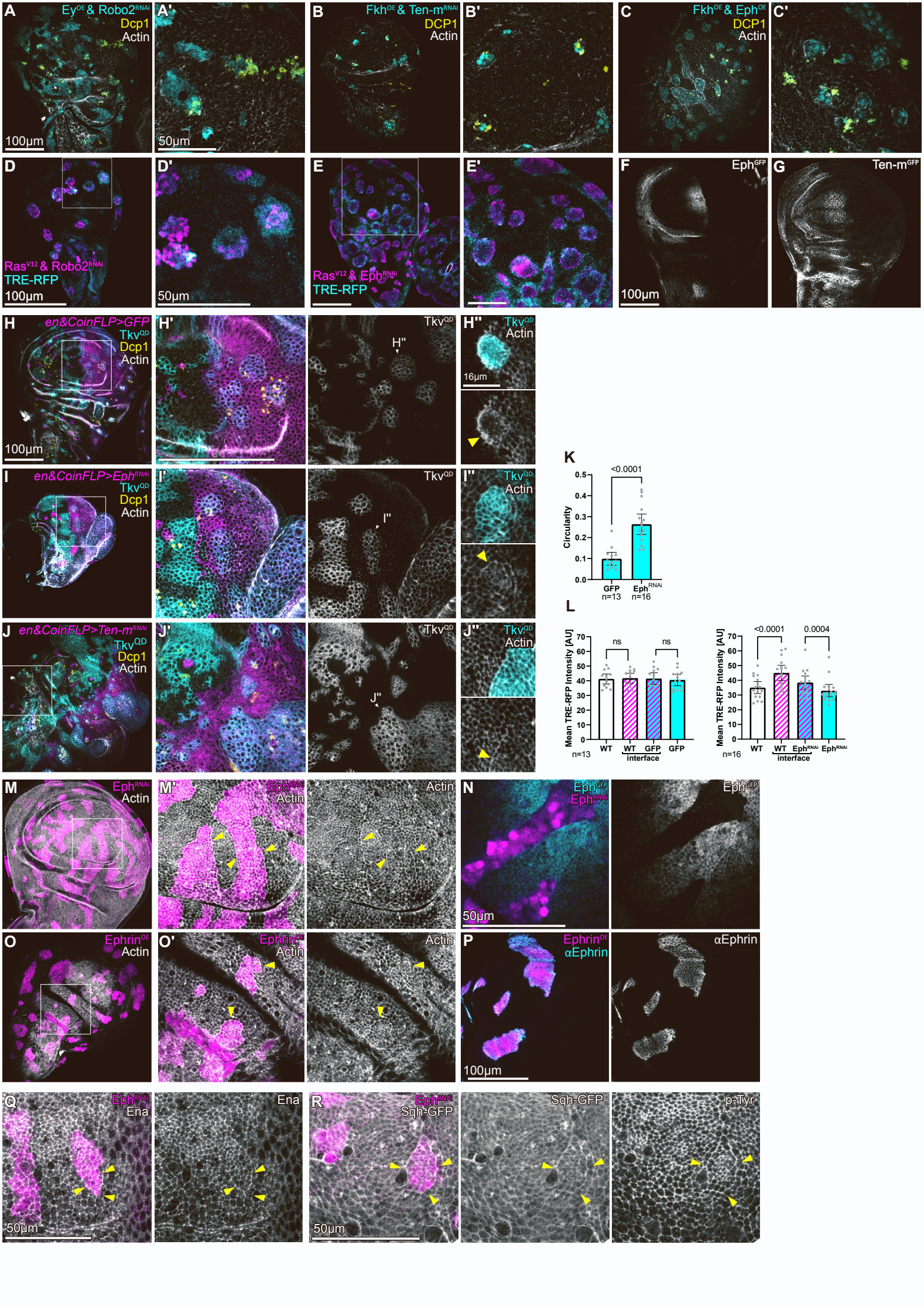
A
Ey^OE & Robo2^RNAi
Dcp1
Actin
100µm
A'
50µm
B
Fkh^OE & Ten-m^RNAi
DCP1
Actin
B'
C
Fkh^OE & Eph^OE
DCP1
Actin
C'
D
Ras^V12 & Robo2^RNAi
TRE-RFP
100µm
D'
50µm
E
Ras^V12 & Eph^RNAi
TRE-RFP
E'
F
Eph^GFP
100µm
G
Ten-m^GFP
H
en&CoinFLP>GFP
Tkv^QD
Dcp1
Actin
100µm
H'
Tkv^QD
H"
H''
Tkv^QD
Actin
16µm
I
en&CoinFLP>Eph^RNAi
Tkv^QD
Dcp1
Actin
I'
Tkv^QD
I"
I''
Tkv^QD
Actin
J
en&CoinFLP>Ten-m^RNAi
Tkv^QD
Dcp1
Actin
J'
Tkv^QD
J"
J''
Tkv^QD
Actin
K
<0.0001
Circularity
0.5
0.4
0.3
0.2
0.1
0.0
GFP
n=13
Eph^RNAi
n=16
L
Mean TRE-RFP Intensity [AU]
ns
ns
WT
WT
GFP
GFP
interface
n=13
<0.0001
0.0004
WT
WT
Eph^RNAi
Eph^RNAi
interface
n=16
M
Eph^RNAi
Actin
M'
Eph^RNAi
Actin
Actin
N
Eph^GFP
Eph^RNAi
50µm
Eph^GFP
O
Ephrin^OE
Actin
O'
Ephrin^OE
Actin
Actin
P
Ephrin^OE
αEphrin
100µm
αEphrin
Q
Eph^RNAi
Ena
50µm
Ena
R
Eph^RNAi
Sqh-GFP
50µm
Sqh-GFP
p-Tyr

Figure S7. Interface surveillance is redundantly mediated by multiple cell surface receptors. Related to Figure 6 and 7 and Data S4.

A-C Mosaic wing discs with clones deregulating a fate-specifying pathway and a cell surface receptor. Knock-down and overexpression constructs for cell surface receptors were selected to restore expression levels of the receptor within aberrant cells to wild type levels. Mosaic clones deregulating a fate-specifying pathway either express *UAS-ey* (Ey^{OE}) (A) or *UAS-fkh* (Fkh^{OE}) (B,C). To manipulate expression levels of cell surface receptors, we used *UAS-robo2-RNAi* ($Robo2^{RNAi}$) (A), *UAS-ten-m-RNAi* ($Ten\text{-}m^{RNAi}$) (B) or *UAS-Eph* (Eph^{OE}) (C). Antibody staining against the cleaved effector caspase (cDcp1) visualizes apoptosis (grey or yellow). Phalloidin visualizes cortical F-actin (grey). Basal sections are shown. Please note that clones still acquire a round smooth shape, and induce interface enrichment of actin and apoptosis.
A'-C' Magnified views of the pouch region of the wing disc. Images are shown at the same scale with a scale bar of 50µm.

D,E Mosaic wing discs with clones expressing oncogenic *UAS-RasV12* (Ras^{V12}) (magenta). The same clones either co-express *UAS-robo2-RNAi* ($Robo2^{RNAi}$) (D) or *UAS-eph-RNAi* (Eph^{RNAi}) (E). TRE-RFP expression is reporting JNK pathway activity (cyan). White frames marks regions shown in (D',E'). Please note that clones still acquire a round smooth shape and induce interface JNK signaling. Image sets are shown at the same scale in (D,E) and (D',E').

F, G Wing disc from larva with the genotype *CoinFLP-LexA::GAD.GAL4/hsflp^{122} ; en-GAL4/tub>CD2>GAL4, UAS-nLac ; UAS-eph-RNAi/eph-GFP* (F) for testing the genetic constructs used in (I), or a disc from larva with the genotype *CoinFLP-LexA::GAD.GAL4/+ ; en-GAL4/+ ; UAS-ten-m-RNAi/ten-m-GFP* (G) for testing the genetic constructs used in (J). No heat shock was applied hence only *en*-GAL4 is active in the posterior compartment. Please note downregulation of Eph (grey) and Ten-m (grey) in the posterior compartments indicating efficient RNAi-mediated knock-down.

H-J Mosaic wing discs with clones deregulating a fate-specifying pathway by expressing a constitutively active Tkv receptor (Tkv^{QD}) via the LexA/LexO-CoinFLP system (grey or cyan). *en*-GAL4 constitutively drives expression of UAS-constructs in the posterior compartment (magenta). The CoinFLP induces either LexA or GAL4 clones upon Flp-FRT recombination. Therefore GAL4/UAS clones expressing *UAS-GFP* (GFP) can also occasionally be observed in the anterior compartment. All GAL4-expressing cells (magenta) drive knock-down of cell surface molecules by expression of *UAS-eph-RNAi* (Eph^{RNAi}) (I) *or UAS-ten-m-RNAi* ($Ten\text{-}m^{RNAi}$) (J). Antibody staining against the cleaved effector caspase (cDcp1) visualizes apoptosis (grey or yellow). Phalloidin visualizes cortical F-actin (grey). White frames mark regions shown in (H'-J'). Images are shown at the same scale in (H-J) and (H'-J'). Representative wing discs of $n \geq 5$ wing discs from $n = 2$ experimental replicates are shown.

H''-J'' Magnified view of clones in the posterior compartment marked in (H'-J'). An apical section is shown. Please note the actin enrichment at clonal interfaces (yellow arrows). Images are shown at the same scale.

K Graph depicting circularity observed for individual *UAS-GFP* (GFP) and *UAS-eph-RNAi* (Eph^{RNAi}) expressing clones. Sample number (n) for individual wing discs and p-values of a two tailed, unpaired t-test are displayed in graphs. Error bars represent mean and 95% confidence interval.

L Graphs depicting mean fluorescence intensity of TRE-RFP reporter in zones of measurement around clones, as depicted in (**Figure 3F**). Graphs display results for mosaic discs with *UAS-GFP* labeled clonal cells (left) or containing *UAS-eph-RNAi* (Eph^{RNAi}) expressing clones (right). Sample number (n) for individual wing discs and p-values of a repeated measured one-way ANOVA with Tukey's multiple comparisons test are displayed in graphs. Error bars represent mean and 95% confidence interval.

M Mosaic wing disc carrying clones expressing *UAS-eph-RNAi* (Eph^{RNAi}) (magenta) to induce downregulation of Eph-receptor. Please note enrichment of F-actin at the clone interface (yellow arrows). White frame marks region shown in (M').

N A wing disc expressing *eph-GFP* (Eph^{GFP}) and carrying mosaic clones *UAS-eph-RNAi* (Eph^{RNAi}) to induce downregulation of the Eph-receptor. Please note the strong downregulation of Eph in clones, demonstrating efficiency of knock-down using *UAS-eph-RNAi* (Eph^{RNAi}).

O Mosaic wing disc carrying clones expressing UAS-ephrin ($Ephrin^{OE}$) to express high levels of Ephrin. An apical section is shown. Please note enrichment of F-actin at the clone interface (yellow arrows). White frame marks region shown in (O').

P Mosaic wing disc with clones expressing *UAS-ephrin* ($Ephrin^{OE}$) and stained with an antibody against Ephrin (αEphrin).

Q, R Mosaic wing discs carrying clones expressing *UAS-eph-RNAi* (Eph^{RNAi}) (magenta) to induce downregulation of Eph-receptor. Please note enrichment of Enabled (Ena) (Q) and the Myosin II regulatory light chain (Sqh-GFP), as well as phosphorylated Tyrosine (pTyr) (R) at the clone interface (yellow arrows).

Table S1

Figure	Genotype	Heat shock	Analysis after:
1A	*hsflp^{122}/+ ; TRE-RFP/+ ; act>y^{+}>GAL4, UAS-GFP/+*	10 min	48 h 25 °C
1B	*hsflp^{122}/UAS-fkh-3xHA ; TRE-RFP/+ ; act>y^{+}>GAL4, UAS-GFP/+*	10 min	30 h 25 °C
1C	*hsflp^{122}/+ ; TRE-RFP/+ ; act>y^{+}>GAL4, UAS-GFP/UAS-tkv^{CA}*	9 min	30 h 25 °C
1D	*hsflp^{122}/+ ; TRE-RFP/UAS-robo3-HA ; act>y^{+}>GAL4, UAS-GFP/+*	10 min	48 h 25°C
1E	*hsflp^{122}/+ ; TRE-RFP/UAS-robo2-HA ; act>y^{+}>GAL4, UAS-GFP/+*	8 min	48 h 25°C
1F	*hsflp^{122}/+ ; TRE-RFP/+ ; act>y^{+}>GAL4, UAS-GFP/UAS-robo2-RNAi*	10 min	48 h 25°C
1G	*hsflp^{122}/+ ; TRE-RFP/UAS-DEphrin ; act>y^{+}>GAL4, UAS-GFP/+*	10 min	30 h 25 °C
1H	*hsflp^{122}/+ ; TRE-RFP/+ ; act>y^{+}>GAL4, UAS-GFP/UAS-eph-RNAi*	7min	72h 25°C
1I	*hsflp^{122}/+ ; TRE-RFP/UAS-ten-a ; act>y^{+}>GAL4, UAS-GFP/+*	10min	48 h 25 °C
1J	*hsflp^{122}/+ ; TRE-RFP/UAS-ten-m ; act>y^{+}>GAL4, UAS-GFP/+*	10min	48 h 25 °C
1K	*hsflp^{122}/+ ; TRE-RFP/+ ; act>y^{+}>GAL4, UAS-GFP/UAS-ft*	10 min	48 h 25 °C
1L	*hsflp^{122}/+ ; TRE-RFP/+ ; act>y^{+}>GAL4, UAS-GFP/UAS-ft-RNAi*	10 min	48 h 25 °C
1M	*hsflp^{122}/+ ; TRE-RFP/UAS-ds^{A} ; act>y^{+}>GAL4, UAS-GFP/+*	10 min	48 h 25°C
1N	*hsflp^{122}/+ ; TRE-RFP/UAS-ds-RNAi ; act>y^{+}>GAL4, UAS-GFP/+*	10 min	48 h 25 °C
S1A	*hsflp^{122}/+ ; TRE-RFP/+ ; act>y^{+}>GAL4, UAS-GFP/+*	9 min	30 h 25 °C
S1B	*hsflp^{122}/UAS-fkh-3xHA ; TRE-RFP/+ ; act>y^{+}>GAL4, UAS-GFP/+*	10 min	30 h 25 °C
S1C	*hsflp^{122}/+ ; TRE-RFP/UAS-ey ; act>y^{+}>GAL4, UAS-GFP/+*	10 min	30 h 25 °C
S1D	*hsflp^{122}/+; TRE-RFP/+; act>y^{+}>GAL4, UAS-GFP/UAS-tkv^{CA}*	9 min	30 h 25 °C

S1E	*hsflp^{122}/+ ; TRE-RFP/dad^{4}-LacZ ; act>y^{+}>GAL4, UAS-GFP/+*	8.5 min	30 h 25°C
S1F	*Flylines from table S1 and S2 were crossed into flies with the genotype hsflp^{122} ; TRE-RFP ; act>y^{+}>GAL4, UAS-GFP*	10min	48 h 25 °C
S1G	*hsflp^{122}/+ ; TRE-RFP/UAS-toll-8 ; act>y^{+}>GAL4, UAS-GFP/+*	10 min	48 h 25 °C
S1H	*hsflp^{122}/+ ; TRE-RFP/+ ; act>y^{+}>GAL4, UAS-GFP/UAS-toll-2*	10 min	48 h 25 °C
S1I	*hsflp^{122}/+ ; TRE-RFP/UAS-netB-RNAi ; act>y^{+}>GAL4, UAS-GFP/+*	10 min	48 h 25 °C
S1J	*hsflp^{122}/+ ; TRE-RFP/UAS-trn-HA ; act>y^{+}>GAL4, UAS-GFP/+*	10 min	30 h 25 °C
3A	*hsflp^{122}/+ ; TRE-RFP/+ ; act>y^{+}>GAL4, UAS-GFP/+*	12 min	30 h 25°C
3B	*hsflp^{122}/+ ; TRE-RFP/UAS-robo2-HA ; act>y^{+}>GAL4, UAS-GFP/+*	12 min	30 h 25°C
3C	*hsflp^{122}/+ ; TRE-RFP/+ ; act>y^{+}>GAL4, UAS-GFP/UAS-robo2-RNAi*	14 min	30 h 25°C
S3B	*hsflp^{122}/+ ; TRE-RFP/+ ; act>y^{+}>GAL4, UAS-GFP/+*	8 min	48 h 25°C
S3C	*hsflp^{122}/+ ; TRE-RFP/UAS-robo2-HA ; act>y^{+}>GAL4, UAS-GFP/+*	8 min	48 h 25°C
S3D	*hsflp^{122}/+ ; TRE-RFP/robo2-GFP ; act>CD2>GAL4, UAS-RFP/puc$^{A251.1F3}$>LacZ*	11 min	30 h 25°C
S3E	*hsflp^{122}/CoinFLP-LexA::GAD.GAL4 ; TRE-RFP/robo2-GFP ; UAS-robo2-RNAi/UAS-LacZ*	14 min	30 h 25°C
4A	*hsflp^{122}/+ ; sqh-GFP/UAS-robo2-HA ; act>CD2>GAL4, UAS-RFP/+*	10 min	30 h 25°C
4B	*hsflp^{122}/+ ; sqh-GFP/UAS-robo2-HA ; act>CD2>GAL4, UAS-RFP/+*	10 min	30 h 25°C
4C	*hsflp^{122}/+ ; sqh-GFP/UAS-robo2-HA ; act>CD2>GAL4, UAS-RFP/+*	10 min	30 h 25°C
4D	*hsflp^{122}/+ ; sqh-GFP/UAS-robo2-HA ; act>CD2>GAL4, UAS-RFP/+*	10 min	30 h 25°C
4E	*hsflp^{122}/+ ; TRE-RFP/+ ; act>y^{+}>GAL4, UAS-GFP/UAS-HA-robo2.DeltaC*	10 min	30 h 25°C
4F	*hsflp^{122}/+ ; TRE-RFP/+ ; act>y^{+}>GAL4, UAS-GFP/UAS-HA-robo2.Delta-Ig1+2 (soure T- Evans)*	10 min	48 h 25°C
4G	*hsflp^{122}/+ ; TRE-RFP/+ ; act>y^{+}>GAL4, UAS-GFP/UAS-sli.D*	10 min	48 h 25°C

4H	*hsflp^{122}/+ ; TRE-RFP/UAS-sli-RNAi ; act>y^{+}>GAL4, UAS-GFP/+*	10 min	30 h 25°C
4I	*hsflp^{122}/+ ; TRE-RFP/+ ; act>y^{+}>GAL4, UAS-GFP/UAS-HA-robo1*	10 min	48 h 25°C
4J	*hsflp^{122}/+ ; TRE-RFP/UAS-robo1-RNAi ; act>y^{+}>GAL4, UAS-GFP/+*	10 min	48 h 25°C
S4C	*hsflp^{122}/+ ; sli-GFP/UAS-sli-RNAi; act>CD2>GAL4, UAS-RFP /+*	10 min	30 h 25°C
S4D	*hsflp^{122}/+ ; TRE-RFP/+ ; act>y^{+}>GAL4, UAS-GFP/UAS-HA-robo1*	10 min	48 h 25°C
S4E	*hsflp^{122}/+ ; UAS-robo1-RNAi/+ ; act>y^{+}>GAL4, UAS-GFP/+*	10 min	48 h 25°C
5A,F	*hsflp^{122}/+ ; TRE-RFP/UAS-robo3-HA ; act>y^{+}>GAL4, UAS-GFP/+*	12 min	30 h 25°C
5B,G	*hsflp^{122}/+ ; TRE-RFP/UAS-robo3-RNAi ; act>y^{+}>GAL4, UAS-GFP/+*	14 min	30 h 25°C
5C	*hsflp^{122}/+ ; TRE-RFP/UAS-robo2-HA ; act>y^{+}>GAL4, UAS-GFP/+*	12 min	30 h 25°C
5D	*hsflp^{122}/+ ; TRE-RFP/+ ; act>y^{+}>GAL4, UAS-GFP/UAS-robo2-RNAi*	14 min	30 h 25°C
5I,J	*hsflp^{122}/+ ; TRE-RFP/UAS-robo3-HA ; act>y^{+}>GAL4, UAS-GFP/UAS-robo2-RNAi*	13 min	48 h 25°C
S5B	*hsflp^{122}/+ ; UAS-robo3-HA/+ ; act>y^{+}>GAL4, UAS-GFP/+*	10 min	30 h 25°C
S5C	*hsflp^{122}/+ ; TRE-RFP/+ ; act>y^{+}>GAL4, UAS-GFP/+*	12 min	30 h 25°C
S5D	*hsflp^{122}/+ ; sqh-GFP/UAS-robo3-HA ; act>CD2>GAL4, UAS-RFP/+*	10 min	30 h 25°C
S5E	elav-GAL4, UAS-GFP/+ ; +/+ ; +/+	No HS	102 h AEL
S5F	elav-GAL4, UAS-GFP/+ ; UAS-robo3-RNAi/+ ; +/+	No HS	102 h AEL
6A,F	*hsflp^{122} ; UAS-Tkv-RNAi/ robo2-GFP ; act>CD2>GAL4, UAS-RFP / +*	18 min	48 h 25°C
6B	*hsflp^{122}/UAS-fkh-3xHA ; robo2-GFP/+ ; act>CD2>GAL4, UAS-RFP/+*	12 min	30 h 25°C
6C	*hsflp^{122}/+ ; robo2-GFP/UAS-ey ; act>CD2>GAL4, UAS-RFP/+*	10 min	30 h 25°C
6H	*hsflp^{122}/+ ; tub>CD2>GAL4, UAS-nLacZ/+ ; eph-GFP/UAS-tkv^{CA}*	10 min	30 h 25°C
6J	*hsflp^{122}/+ ; tub>CD2>GAL4, UAS-nLacZ/+ ; ten-m-GFP/UAS-tkv^{CA}*	10 min	30 h 25°C
6L	*hsflp^{122}/ten-a-GFP ; +/tub>CD2>GAL4, UAS-nLacZ ; UAS-tkv^{CA}/+*	12 min	30 h 25°C

6N	*hsflp^{122} ; UAS-Tkv-RNAi/+ ; act>CD2>GAL4, UAS-RFP / trn-LacZ*	11 min	40 h 25°C
6P	*hsflp^{122}/+ ; robo2-GFP/UAS-Ras^{V12} ; act>CD2>GAL4, UAS-RFP/+*	10 min	30 h 25°C
6R	*hsflp^{122}/+ ; tub>CD2>GAL4, UAS-nLacZ/+ ; eph-GFP/UAS-Ras^{V12}*	10 min	30 h 25°C
6T	*hsflp^{122}/+ ; tub>CD2>GAL4, UAS-nLacZ/+ ; ten-m-GFP/UAS-Ras^{V12}*	10 min	30 h 25°C
6U	*hsflp^{122}/+ ; robo2-GFP/+ ; act>CD2>GAL4, UAS-RFP/+*	9.5 min	30 h 25°C
6V	*hsflp^{122}/+ ; robo2-GFP/+ ; act>CD2>GAL4, UAS-RFP/UAS-myc*	9.5 min	30 h 25°C
6W	*hsflp^{122}/+ ; tub>CD2>GAL4, UAS-nLacZ/+ ; eph-GFP/+*	9.5 min	30 h 25°C
6X	*hsflp^{122}/+ ; tub>CD2>GAL4, UAS-nLacZ/+ ; eph-GFP/UAS-myc*	9.5 min	30 h 25°C
6Y	*hsflp^{122}/+ ; tub>CD2>GAL4, UAS-nLacZ/+ ; ten-m-GFP/+*	9.5 min	30 h 25°C
6Z	*hsflp^{122}/+ ; tub>CD2>GAL4, UAS-nLacZ/+ ; ten-m-GFP/UAS-myc*	9.5 min	30 h 25°C
S6D	*hsflp^{122}/UAS-fkh-3xHA ; +/+ ; act>CD2>GAL4, UAS-RFP/eph-GFP*	10 min	30 h 25°C
S6E	*hsflp^{122}/UAS-fkh-3xHA; tub>CD2>GAL4, UAS-nLacZ/+ ; ten-m-GFP/+*	10 min	30 h 25°C
S6F	*ten-a-GFP/UAS-fkh-3xHA; hsflp^{38}/+ ; act>CD2>GAL4, UAS-RFP/+*	1 h	40 h 25°C
S6G	*hsflp^{122}/+ ; tub>CD2>GAL4, UAS-nLacZ/+ ; eph-GFP/UAS-ci-HA*	10 min	30 h 25°C
S6H	*hsflp^{122}/+ ; tub>CD2>GAL4, UAS-nLacZ/+ ; ten-m-GFP/UAS-ci-HA*	10 min	30 h 25°C
S6I	*hsflp^{122}/ten-a-GFP ; tub>CD2>GAL4, UAS-nLacZ/+ ; UAS-ci-HA/+*	13 min	30 h 25°C
S6J	*hsflp^{122}/+ ; TRE-RFP/+ ; act>y^{+}>GAL4, UAS-GFP/UAS-Ras^{V12}*	9 min	30 h 25°C
S6L	*hsflp^{122}/+ ; +/+ ; act>CD2>GAL4, UAS-RFP/ UAS-Ras^{V12}*	12 min	30 h 25°C
S6N	*hsflp^{122}/ten-a-GFP ; +/+ ; act>CD2>GAL4, UAS-RFP/UAS-Ras^{V12}*	12 min	30 h 25°C
S6P	*hsflp^{122}/+ ; UAS-Ras^{V12}/+ ; act>CD2>GAL4, UAS-RFP/trn-LacZ*	12 min	30 h 25°C
S6R	*hsflp^{122}/+ ; ds-LacZ/+ ; act>y^{+}>GAL4, UAS-GFP/UAS-Ras^{V12}*	10 min	30 h 25°C
S6S	*hsflp^{122}/+ ; robo2-GFP/+ ; act>CD2>GAL4, UAS-RFP/+*	9.5 min	30 h 25°C
S6T	*hsflp^{122}/+ ; robo2-GFP/+ ; act>CD2>GAL4, UAS-RFP/UAS-myc*	9.5 min	30 h 25°C

S6U	*hsflp^{122}/+ ; robo2-GFP/+; act>CD2>GAL4, UAS-RFP/UAS-hpo*	12 min	30 h 25°C
S6V	*hsflp^{122}/+ ; tub>CD2>GAL4, UAS-nLacZ/+ ; eph-GFP/UAS-hpo*	12 min	30 h 25°C
S6W	*hsflp^{122}/+ ; tub>CD2>GAL4, UAS-nLacZ/+ ; ten-m-GFP/UAS-hpo*	12 min	30 h 25°C
S6X	*hsflp^{122}/+ ; tub>CD2>GAL4, UAS-nLacZ/+ ; +/UAS-hpo*	12 min	30 h 25°C
S6Y	*hsflp^{122}/+ ; robo2-GFP/+ ; act>CD2>GAL4, UAS-RFP/UAS-wtsRNAi*	9.5 min	30 h 25°C
S6Z	*hsflp^{122}/+ ; tub>CD2>GAL4, UAS-nLacZ/+ ; eph-GFP/UAS-wtsRNAi*	9.5 min	30 h 25°C
S6AA	*hsflp^{122}/+ ; tub>CD2>GAL4, UAS-nLacZ/+ ; ten-m-GFP/UAS-wtsRNAi*	9.5 min	30 h 25°C
S6AB	*hsflp^{122}/+ ; +/+ ; act>CD2>GAL4, UAS-RFP/UAS-wtsRNAi*	9.5 min	30 h 25°C
S7A	*hsflp^{122}/+ ; UAS-ey/+ ; act>y^{+}>GAL4, UAS-GFP /UAS-robo2-RNAi*	10 min	30 h 25°C
S7B	*hsflp^{122}/UAS-fkh-3xHA ; tub>CD2>GAL4, UAS-nLacZ/+ ; UAS-ten-m-RNAi/+*	10 min	30 h 25°C
S7C	*hsflp^{122}/UAS-fkh-3xHA ; UAS-eph/+ ; act>CD2>GAL4, UAS-RFP/+*	12 min	30 h 25°C
S7D	*hsflp^{122}/+ ; tub>CD2>GAL4, UAS-nLacZ/TRE-RFP ; UAS-robo2-RNAi/UAS-Ras^{V12}*	10 min	30 h 25°C
S7E	*hsflp^{122}/+ ; TRE-RFP/UAS-Ras^{V12} ; act>y^{+}>GAL4, UAS-GFP/UAS-eph-RNAi*	10 min	30 h 25°C
S7F	*CoinFLP-LexA::GAD.GAL4/hsflp^{122} ; en-GAL4/tub>CD2>GAL4, UAS-nLacZ ; UAS-eph-RNAi/eph-GFP*	No HS	108h AEL
S7G	*CoinFLP-LexA::GAD.GAL4/+ ; en-GAL4/+ ; UAS-ten-m-RNAi/ten-m-GFP*	No HS	108h AEL
S7H	*hsflp^{122}/CoinFLP-LexA::GAD.GAL4 ; en-GAL4/UAS-mCD8::GFP, LexO-mCherry::CAAX ; LexO-tkv^{QD}/+*	5 min	38 h 25°C
S7I	*hsflp^{122}/CoinFLP-LexA::GAD.GAL4 ; en-GAL4/UAS-mCD8::GFP, LexO-mCherry::CAAX ; LexO-tkv^{QD}/UAS-eph-RNAi*	5 min	38 h 25°C
S7J	*hsflp^{122}/CoinFLP-LexA::GAD.GAL4 ; en-GAL4/UAS-mCD8::GFP, LexO-mCherry::CAAX ; LexO-tkv^{QD}/UAS-ten-m-RNAi*	5 min	38 h 25°C
S7M	*hsflp^{122}/+ ; +/+ ; act>y^{+}>GAL4, UAS-GFP/UAS-eph-RNAi*	11 min	48h 25°C

S7N	*hsflp^{122}/+ ; tub>CD2>GAL4, UAS-nLacZ/+ ; eph-GFP/UAS-eph-RNAi*	15 min	72 h 25°C
S7O	*hsflp^{122}/+ ; TRE-RFP/UAS-DEphrin ; act>y^{+}>GAL4, UAS-GFP/+*	10 min	30 h 25 °C
S7P	*hsflp^{122}/+ ; UAS-DEphrin /+ ; act>y^{+}>GAL4, UAS-GFP/+*	10 min	30 h 25°C
S7Q	*hsflp^{122}/+ ; sqh-GFP/+ act>CD2>GAL4, UAS-RFP/ UAS-eph-RNAi*	10 min	30 h 25°C
S7P	*hsflp^{122}/+ ; sqh-GFP/+ act>CD2>GAL4, UAS-RFP/ UAS-eph-RNAi*	10 min	30 h 25°C

Table S1. Detailed genotypes per figure panel. Related to STAR methods.

Table S2

S1A’	*Overlay*: apical z-sections of actin and clonal marker. Basal z-sections of TRE-RFP. *Black and white images*: apical z-section of Actin. Basal z-sections of TRE-RFP and Dcp1.
S1B’	*Overlay:* local Z projection of apical actin, apical clonal marker, and apical to lateral TRE-RFP. *Black and white images:* local z projection of apical actin, basal max projection of TRE-RFP and Dcp1
S1C’	*Overlay:* apical z-sections of actin, clonal marker and TRE-RFP. *Black and white images:* apical z-section of actin and lateral z-section of TRE-RFP and Dcp1.
S1D’	*Overlay:* max projection of apical z-sections of actin, clonal marker and TRE-RFP. *Black and white images:* apical z-section of actin, lateral z-section of TRE-RFP and basal z-section of Dcp1.
S5C and S5C’	Basal z-section.
S5C’’	Max projection of 3 apical z-sections.
5A and 5A’	Lateral z-section of clonal marker and TRE-RFP. Basal z-section of Dcp1.
5A’’	Max projection of 3 apical z-sections.
5B and 5B’	Lateral z-section of clonal marker and TRE-RFP. Basal z-section of Dcp1.
5B’’	Max projection of 3 apical z-sections.
3A	Lateral z-section for clonal marker and TRE-RFP (different z-section for pouch and notum). Max projection of z-sections for Dcp1.
3A’ and 3A’’	Max projection of apical z-sections for Actin, a lateral z-section for TRE-RFP and clonal marker and max projection of z-sections for Dcp1.
3C	Lateral z-section.
3C’	Apical z-section for Actin and clonal marker. Lateral z-section for TRE-RFP and Dcp1.
3C’’	Max projection of lateral to basal z-sections.
3B	Basal z-section for TRE-RFP and clonal marker (different z-section for pouch and notum). Max projection of all z-sections for Dcp1.
3B’	max projection of 2 apical z-sections for Actin, TRE-RFP and clonal marker. Basal z-section for Dcp1.
3B’’	max projection of 2 apical z-sections for Actin. Lateral z-section for clonal marker and TRE-RFP. Max projection of all z-sections for Dcp1.
S7H-J	lateral z-section for LexA and Gal4 clonal marker and Actin. Max projection of basal z-sections for Dcp1.
S6J	Max projection of apical to lateral z-section in the hinge
6U-Z and S6S-AB	Local z projection of lateral z-section

Table S2. Selected z-positions for figure panels with overlay of channels from different z-positions. Related to STAR methods.

In most figure panels, individual channels represent the same z-position from a confocal image stack. However, some panels may assemble channels from different z-position in the wing disc (details below). Such a portrayal was chosen to better visualize the spatially distinct phenotypes at different z-positions within the tissue, specifically of (1) junctional actin (apical), (2) cytoplasmic/nuclear RFP (lateral) and (3)

cDcp1 (basal) in one image panel. This was meant to reduce the data load in the manuscript that would be otherwise required to visualize all channels at all z-positions. All full original image stacks are of course available upon request.